JM PAPERS

Resolvent analysis of turbulent flow laden with low-inertia particles

Rasmus Korslund Schlander[1], Stelios Rigopoulos[2] and George Papadakis[1],†

[1]Department of Aeronautics, Imperial College London, London SW7 2AZ, UK

[2]Department of Mechanical Engineering, Imperial College London, London SW7 2AZ, UK

We extend the resolvent framework to two-phase flows with low-inertia particles. The particle velocities are modelled using the equilibrium Eulerian model. We analyse the turbulent flow in a vertical pipe with Reynolds number of 5300 (based on diameter and bulk velocity), for Stokes numbers $St^+ = 0 - 1$, Froude numbers $Fr_z = -4, -0.4, 0.4, 4$ and $1/Fr_z = 0$ (gravity omitted). The governing equations are written in input–output form and a singular value decomposition is performed on the resolvent operator. As for single-phase flows, the operator is low rank around the critical layer, and the true response can be approximated using one singular vector. Even with a crude forcing model, the formulation can predict physical phenomena observed in Lagrangian simulations, such as particle clustering and gravitational effects. Increasing the Stokes number shifts the predicted concentration spectra to lower wavelengths; this shift also appears in the direct numerical simulation spectra and is due to particle clustering. When gravity is present, there are two critical layers, one for the concentration field, and one for the velocity field. For upward flow, the peak of concentration fluctuations shifts closer to the wall, in agreement with the literature. We explain this with the aid of the different locations of the two critical layers. Finally, the model correctly predicts the interaction of near-wall vortices with particle clusters. Overall, the resolvent operator provides a useful framework to explain and interpret many features observed in Lagrangian simulations. The application of the resolvent framework to higher St^+ flows in combination with Lagrangian simulations is also discussed.

Key words: pipe flow, particle/fluid flow, computational methods

† Email address for correspondence: g.papadakis@imperial.ac.uk

R.K. Schlander, S. Rigopoulos and G. Papadakis

1. Introduction

Inertial particles in wall-bounded flows and their interaction with turbulence and coherent structures have long been investigated both experimentally and numerically. One of the key effects of inertia is that it prevents particles from following highly turbulent motion, which leads to preferential concentration. This was observed for the first time in the numerical simulations by Squires & Eaton (1991), and it is sometimes referred to as the particle centrifuge effect. Another important phenomenon of inertial particles in wall-bounded flows is turbophoresis, which denotes the transport of particles from the bulk of the flow to the near-wall region; see Caporaloni *et al.* (1975) and Reeks (1983). Gravity also affects particle movement and deposition; this has been investigated numerically in Uijttewaal & Oliemans (1996), Marchioli, Picciotto & Soldati (2007), Nilsen, Andersson & Zhao (2013) and experimentally among others in Oliveira, Van Der Geld & Kuerten (2017) and Fong, Amili & Coletti (2019). More information on particle transport in turbulent flows can be found in the review papers by Balachandar & Eaton (2010) and Brandt & Coletti (2022).

The predominant method to simulate particle-laden flows is based on Lagrangian tracking of a very large number of point particles. The equation of motion of Maxey & Riley (1983) is integrated and momentum is exchanged between the two phases. The interaction can be one-way (very dilute suspensions), two-way (relatively low volume fraction, but high mass loading) or four-way coupled (dense suspensions in terms of volume fraction). For low-inertia particles with Stokes number based on the Kolmogorov scale, $St_k \lesssim 1$, Eulerian formulations are also applicable (see figure 1 in Balachandar & Eaton 2010) that solve separate momentum and concentration equations for the particulate phase (two-fluid approach); see Guha (2008) and Fox, Laurent & Massot (2008). For particles with even smaller inertia, $St_k \lesssim 0.2$–0.6, the equilibrium Eulerian model is applicable. The model is formally derived from the particle equation of motion using Taylor series expansion in terms of St_k, see Maxey (1987), Druzhinin (1994) and Ferry & Balachandar (2001) for a more general form.

The equilibrium Eulerian model, when applicable, is computationally more efficient and easier to implement compared with the Lagrangian approach since it requires only the local flow velocity field and its derivatives to compute the particle velocity. It can also accommodate more easily polydisperse distributions compared with full Eulerian models, and can capture the turbophoresis effect that is known to lead to preferential particle concentration near the wall, see Balachandar & Eaton (2010) for details. The equilibrium Eulerian model has been applied to both laminar and turbulent flows. For example, Pilou *et al.* (2011) analysed the deposition of inertial particles in a $90°$ pipe bend for a laminar flow, Icardi *et al.* (2013) simulated polydisperse particles in a turbulent channel flow using large eddy simulations (LES), Cerminara, Esposti Ongaro & Berselli (2016) examined a volcanic ash plume using LES, Yang *et al.* (2016) analysed bubbles in a jet using LES, Aiyer *et al.* (2019) simulated oil droplets in a cross-flow jet and, finally, Balachandar *et al.* (2020) suggested this as a method to simulate host-to-host airborne transmission of Covid-19 to establish social distancing guidelines.

The description of particulate flows in an Eulerian framework opens new directions of analysis wherein tools that have been developed for single-phase flows can be directly applied to two-phase flows. In this context, proper orthogonal decomposition (POD) and extended POD were applied recently to characterise the concentration field of low-inertial particles inside turbulent pipe flow (Schlander, Rigopoulos & Papadakis 2024). A new Fukagata–Iwamoto–Kasagi identity was also derived to quantify the rate of particle deposition on the pipe wall, and terms that arise due to the effect of turbophoresis appeared naturally.

In the present paper, we consider the application of resolvent analysis for two-phase flows. This is an equation-driven approach, where the governing equations of the fluctuations are Fourier transformed in time (and also space if there are homogeneous directions) and put into an input (forcing)-output (response) form. The nonlinear terms act as forcing to the system. The fluctuations are defined with respect to a time-average field, which is considered known. A singular value decomposition (SVD) is performed on the resolvent operator that relates the input to the output in the frequency domain. The SVD provides the most amplified response modes and the corresponding forcing shapes. In the presence of shear, for example in wall-bounded flows, the operator is low rank (in the sense that the first singular value is orders of magnitude larger than the rest). This feature can be exploited to derive a compact description of the underlying fluctuation field which can be used to provide a low-order representation of the key dynamical processes of turbulence. This approach was proposed by McKeon & Sharma (2010) for single-phase incompressible flows and since then has proven to be a useful framework to probe and analyse turbulent shear flows, see the review of McKeon (2017) for more details. Most importantly, the resolvent operator can be derived analytically and this allows the derivation of new scaling relations directly from the governing equations, see for example Moarref *et al.* (2013). This approach has been extended to supersonic boundary layers (Ahmed *et al.* 2021), control applications (Luhar, Sharma & McKeon 2014; Yeh & Taira 2019) and flow estimation (Thomareis & Papadakis 2018; Morra *et al.* 2019; Martini *et al.* 2020; Towne, Lozano-Durán & Yang 2020). The statistics of the forcing term were investigated in Morra *et al.* (2021).

In the above context, the central aim of this paper is to derive the resolvent operator for a turbulent flow laden with low-inertia particles and analyse the effects of inertia and gravity on particle behaviour. For simplicity, we use the Eulerian equilibrium model to obtain the particle velocity field. We explore questions such as, is the resolvent operator low rank? Can it predict particle clustering? What additional physical insight it can bring to explain the effect of inertia and gravity on the particle concentration and its spectra?

Looking at the bigger picture, there is an even more important question to consider. The Eulerian equilibrium model is valid only for low-inertia particles with $St_k \lessapprox 0.2$–0.6. Can the resolvent framework (which is based on an Eulerian description of the flow) be applied to larger particles, where only Lagrangian simulations provide accurate results? In other words, can we bridge the two descriptions? We believe that the answer to the above questions is yes, and we provide some thoughts on this at the end of the paper.

The article is structured as follows: the modelling approach, cases examined (including validation) and mean concentration characteristics are presented in §§ 2–4, respectively. The resolvent operator is derived in § 5 and results are presented in § 6. We summarise the main findings of the paper and discuss directions for future research in § 7.

2. Modelling of turbulent flow with low-inertia particles

We consider the turbulent flow inside a circular pipe with low-inertia particles injected at the inlet. The flow is assumed to be incompressible and the mass fraction of the particles is very small, i.e. the suspension is dilute and the presence of the particles does not affect the flow (one-way coupling). The continuity and momentum equations therefore take the

standard form and can be written in Cartesian tensor notation as

$$\frac{\partial u_i}{\partial x_i} = 0, \tag{2.1a}$$

$$\frac{\partial u_i}{\partial t} + \frac{\partial u_i u_j}{\partial x_j} = -\frac{\partial p}{\partial x_i} + \frac{1}{Re}\frac{\partial^2 u_i}{\partial x_j \partial x_j}, \tag{2.1b}$$

where u_i is the instantaneous fluid velocity in the ith direction, p is the pressure and t is the time. The notation (x_1, x_2, x_3) for the spatial coordinates is used interchangeably with the notation (x, y, z), where $z = x_3$ is the axial (streamwise) direction. Due to rotational symmetry, it is also convenient to use polar coordinates (r, θ, z), where $(x, y) = (r \cos \theta, r \sin \theta)$. Velocities are non-dimensionalised with the bulk velocity U_B, and distances with the pipe diameter D. The Reynolds number is defined as $Re = U_B D/\nu$, where ν is the kinematic viscosity. The mean, i.e. time-average, and fluctuating quantities are denoted by an overbar and a prime, respectively, for example, $\overline{u_i}$ and u_i'.

Eulerian theories for particle deposition in turbulent flows have been proposed; see Guha (1997) and Young & Leeming (1997) and refer also to Guha (2008) for a review. The theories are based on the formulation of partial differential equations for the momentum and continuity equations for the particle phase. In order to simplify the resulting system, here, we obtain the particle velocity field explicitly from the fluid velocity using the equilibrium Eulerian model of Ferry & Balachandar (2001). The model is briefly described below; more details are provided in the aforementioned reference.

We assume that the diameter of the particles is much smaller than the Kolmogorov length scale and there are no inter-particle collisions. Furthermore, it is assumed that Stokes drag and gravity are the only forces acting on the particles. Under these conditions, the equation of motion becomes

$$\frac{\mathrm{D}v_i^*}{\mathrm{D}t^*} = \frac{1}{\tau}(u_i^* - v_i^*) + g_i, \tag{2.2}$$

where t^* is the dimensional time, $\mathrm{D}/\mathrm{D}t^*$ is the derivative along the particle trajectory, u_i^*, v_i^*, g_i are the dimensional fluid velocity, particle velocity and gravitational acceleration in the ith direction, respectively. The particle relaxation time, τ, is defined as

$$\tau = \frac{\rho_\mathrm{p} d_p^2}{18\mu_f}, \tag{2.3}$$

where ρ_p, d_p are the particle density and diameter, respectively, and ρ_f, μ_f are the fluid density and dynamic viscosity, respectively. In the present simulations, we take $\rho_p/\rho_f \approx 1000$. If τ is small, v_i^* can be expanded in Taylor series as (see Maxey 1987)

$$v_i^* = v_i^{(0)} + v_i^{(1)}\tau + v_i^{(2)}\tau^2 + \cdots. \tag{2.4}$$

Substituting in (2.2), equating terms with the same order of τ and retaining only the linear term we arrive at

$$v_i^* = u_i^* - \tau \left(\frac{\mathrm{D}u_i^*}{\mathrm{D}t^*} - g_i \right). \tag{2.5}$$

This expression implies that the particle velocity field $v_i^*(\mathbf{x}, t)$ is unique and continuous, and it is determined solely by the fluid velocity and its derivatives. Incidentally, the same

result can also be obtained from (2.2) assuming that the particle and velocity accelerations are approximately equal. For small enough τ, the effect of initial conditions (that results in non-unique solutions) can be neglected because it decays exponentially. The exact condition under which this is satisfied is derived in Ferry & Balachandar (2001). More complicated expressions that account for other forces in the equation of motion and include quadratic terms in the expansion can be found in Ferry & Balachandar (2001). For the purposes of the current investigation, however, (2.5) suffices.

The particle concentration $c^*(\boldsymbol{x}, t)$ is defined as the volume of particles per unit volume of fluid; this is also a continuous field. The transport equation for $c^*(\boldsymbol{x}, t)$ is

$$\frac{\partial c^*}{\partial t^*} + \frac{\partial v_j^* c^*}{\partial x_j^*} = \frac{\partial}{\partial x_j}\left(D_p \frac{\partial c^*}{\partial x_j^*}\right), \qquad (2.6)$$

where D_p is the particle Brownian diffusion coefficient given by the Einstein relation $D_p = R_p T \tau$, with T being the temperature (assuming isothermal conditions), $R_p = k/m_p$, where k is Boltzmann's constant and $m_p = \pi d_p^3 \rho_p/6$ is the mass of the particle. The reference quantity for $c^*(\boldsymbol{x}, t)$ is the particle concentration at the pipe inlet, c_I, i.e. $c(\boldsymbol{x}, t) = c^*(\boldsymbol{x}, t)/c_I$. Defining $Sc = \nu/D_p$ as the particle Schmidt number, we obtain the particle concentration equation in non-dimensional form

$$\frac{\partial c}{\partial t} + \frac{\partial v_j c}{\partial x_j} = \frac{1}{ReSc}\frac{\partial^2 c}{\partial x_j \partial x_j}. \qquad (2.7)$$

Using air properties at room temperature and micron-size solid particles (see for example table 2 in Pilou *et al.* 2011), the value of D_p is computed to be several orders of magnitude smaller than ν, thus $Sc \gg 1$. Very high values of Sc result in Batchelor scales that are much smaller than the Kolmogorov scale (their ratio scales as $Sc^{-0.5}$) that are computationally expensive to resolve. On the other hand, under-resolution of these scales introduces numerical artefacts in the particle concentration field, such as over- and under-shoots, necessitating the introduction of a total variation diminishing scheme, or some other form of filtering such as spectral filtering of high wavenumbers as in Ferry & Balachandar (2002) and Rani & Balachandar (2003). To avoid the excessive cost of simulation or the need to employ a filtering scheme, we adopt a compromise approach, where the Schmidt number is set to $Sc = 1$. In Richter & Chamecki (2018), Sc was also set to unity, while in the LES simulations of Yang *et al.* (2016) and Aiyer *et al.* (2019) molecular diffusion was neglected but an eddy diffusivity model was employed for the sub-grid-scale concentration fluxes.

Inserting the non-dimensional form of (2.5) into (2.7) we obtain

$$\frac{\partial c}{\partial t} + \frac{\partial}{\partial x_j}\left\{\left[u_j + St\left(\frac{1}{Fr_j} - \frac{\partial u_j}{\partial t} - u_k\frac{\partial u_j}{\partial x_k}\right)\right]c\right\} = \frac{1}{ReSc}\frac{\partial^2 c}{\partial x_j \partial x_j}, \qquad (2.8)$$

where $Fr_i = U_B^2/g_i D$ and $St = \tau U_B/D$ are the Froude and Stokes numbers, respectively (based on global variables). When $Fr_z > 0$, gravity is aligned with the mean streamwise velocity, corresponding to downward flow in a vertical pipe. Similarly, when $Fr_z < 0$, the flow is moving upwards in a vertical pipe.

The flow is driven by a constant streamwise pressure gradient. Standard boundary conditions are used for velocities, i.e. periodic conditions at the inlet/outlet planes and no slip at the wall. Particles are inserted at the inlet of the pipe with uniform concentration $c(r, \theta, 0) = 1$. At the exit, a non-reflecting boundary condition is employed, $\partial c/\partial t + \partial v_z c/\partial z = 0$, where $v_z(r, \theta, L)$ is the local instantaneous axial particle velocity.

Domain length	Re_τ	N_c	Δr^+_{wall}	$(\Delta\theta R)^+_{wall}$	Δr^+_{max}	Δz^+	$\Delta t[R/U_B]$
7.5D	180	8.8×10^6	0.35	3.75	2.29	5.25	0.008
15D	180	2×10^7	0.1	3.75	2.29	5.25	0.008
7.5D	323	25.6×10^6	0.1	4.84	2.63	8.2	0.004

Table 1. Grid parameters for the pipe flow simulations.

We assume a totally absorbing wall, i.e. the particles deposit upon impact. The commonly applied boundary condition for this case is $c(R, \theta, z) = 0$, but this is only approximately correct for very small particles transported to the wall by Brownian diffusion and zero convective velocity; see Lee, Hanratty & Adrian (1989). A more general boundary condition valid in the diffusion–impaction deposition regime was derived in Young & Leeming (1997) using kinetic theory. This boundary condition links the particle wall-normal velocity $v_r(R, \theta, z)$ with the wall concentration $c(R, \theta, z)$ and the radial derivative $(\partial c/\partial r)(R, \theta, z)$. In our case, the time-average radial particle velocity computed from (2.5) is

$$\bar{v}_r = -St \left(\frac{\partial \overline{u'^2_r}}{\partial r} + \frac{\overline{u'^2_r} - \overline{u'^2_\theta}}{r} \right), \tag{2.9}$$

which is equal to 0 at the wall, thus we have used the boundary condition $c(R, \theta, z) = 0$. Note that, away from the wall, $\bar{v}_r(r, \theta, z) \neq 0$ and the model captures the turbophoretic effect, i.e. the mean particle drift towards the wall (close to the wall $\partial \overline{u'^2_r}/\partial r < 0$ and $|\partial \overline{u'^2_r}/\partial r| > |\overline{u'^2_r} - \overline{u'^2_\theta}|/r$, thus $\bar{v}_r > 0$); see also Picano, Sardina & Casciola (2009) and Ferry & Balachandar (2001).

3. Computational details and validation

We perform direct numerical simulations (DNS) of a fully developed turbulent flow in a pipe. The Reynolds number is $Re = 5300$, which corresponds to $Re_\tau = u_\tau R/\nu = 180$, where u_τ is the friction velocity and R is the radius. An H-type grid is employed around the centre of the pipe that transitions to O-type closer to the wall to fit the cylindrical boundary. The computational domain spans $L = 7.5D$, large enough to resolve the largest coherent structures according to the recommendations of Wu & Moin (2008). The cross-section is discretised with $N_{c,cross} = 1.7 \times 10^4$ cells and $N_z = 512$ layers are employed in the streamwise direction, resulting in a total of $N_c = 8.8 \times 10^6$ cells. The ratio of the local grid size (computed as the cubic root of the cell volume) to the Kolmogorov length scale $\eta = (\nu^3/\epsilon)^{0.25}$, is less than 1.8 in most parts of the domain, thus the flow is overall well resolved (Pope 2000). The time step is $\Delta t = 0.008(R/U_B)$, corresponding to a maximum Courant–Friedrichs–Lewy (CFL) number of 0.6. Grid spacings in terms of wall units in the radial, azimuthal and axial directions are provided in table 1.

Two additional pipe flow simulations were also performed; one with pipe length $L = 15D$ and 50 % more cells in the range $r = 0.5R - R$ at the same $Re = 5300$, and one at $Re = 10\,300$ ($Re_\tau = 323$); see also table 1 for more details. For the $L = 7.5D$ pipe length case, the particles are reinserted from the outlet to the inlet to artificially increase the length to $15D$ to ensure that the mean concentration profiles become self-similar. The profiles are validated against the $L = 15D$ case; more details are provided in § 4.

The governing equations are solved using our in-house unstructured finite volume solver, Pantarhei; see Mikhaylov, Rigopoulos & Papadakis (2021), Yao, Mollicone & Papadakis (2022), Schlander, Rigopoulos & Papadakis (2022) and Yao & Papadakis (2023). The convection and diffusion terms are discretised using a second-order central approximation. A third-order backward difference scheme is employed for the transient term. Orthogonal diffusion terms are treated implicitly, while the convection and non-orthogonal diffusion terms are treated explicitly using third-order extrapolation in time. The fractional step method is employed to correct velocities and pressure to satisfy the continuity equation at the end of each time step. The resulting linear systems are solved with the generalized minimal residuals (GMRES) iterative algorithm implemented in the PETSc library (Balay *et al.* 2022). Convergence is accelerated using an algebraic multigrid pre-conditioner from the Hypre library (Falgout & Yang 2002).

After the flow has reached a statistically steady state, statistics are collected over 20 000 time steps, corresponding to $160(R/U_B)$. Averaging was taken in time and in both homogeneous directions (axial and azimuthal). Validation of the flow field for $Re = 5300$ can be found in Schlander *et al.* (2022). Mean and root-mean-square (r.m.s.) velocity profiles for $Re = 10\,300$ are compared against the DNS of Veenman (2004) and the experiments of Oliveira, Van Der Geld & Kuerten (2013) in panels (*a*) and (*b*) of figure 1. Overall, there is very good agreement with the results from the literature.

For the particle phase, we define the Stokes number based on wall units as $St^+ = \tau u_\tau^2/\nu$. Comparisons of the time-average particle velocity field obtained from (2.5) against the Lagrangian simulations of Ferry, Rani & Balachandar (2003) for a turbulent channel flow at $Re_\tau = 180$ are reported in Schlander *et al.* (2024). The results match very well for both wall-normal and streamwise velocities for $St^+ = 1$, but differences appear (mainly in the streamwise velocity) for $St^+ = 3$. We have also performed additional validation against experiments for the particle velocity for pipe flow, the geometry pertinent for this paper. In figure 1(*c*) the time-average streamwise particle velocity is compared with the experiments of Oliveira *et al.* (2017) for downward flow for $St^+ = 0.1$ and $St^+ = 1.56$. There is excellent agreement between the two sets of data. The results show that the equilibrium Eulerian model provides sufficiently accurate particle velocity fields for $St^+ \leq 1$.

4. Mean concentration characteristics

In total, 20 flow configurations were simulated for $St^+ = 0.1, 0.2, 0.5, 1.0$ ($St = 0.004, 0.008, 0.02, 0.04$) and $Fr_z = -4, -0.4, 0.4, 4$ as well as the special case with no gravity ($Fr_z \to \infty$). The range of the Stokes numbers is based on the limitations of the equilibrium Eulerian model mentioned in the previous section, while the Froude numbers are in the same range as Marchioli *et al.* (2007) and Fong *et al.* (2019), where $Fr_z \sim \mathcal{O}(10)$.

Radial concentration profiles for two St^+ are plotted at different streamwise locations in the range $z = 8D$–$15D$ in figure 2. The profiles become self-similar for $z \geq 12D$; this length is almost independent of St^+. Results from the larger domain $L = 15D$, denoted by circles in panels (*a*) and (*d*), match the results of the shorter domain and confirm the self-similarity and its starting location.

In figure 3(*a*), mean particle concentration profiles at $z = 14D$ are plotted for $St^+ = 0.1, 0.2, 0.5, 1.0$, $Fr_z = \pm 4$ and no gravity. For $St^+ \ll 1$, the expected profile of a passive scalar that peaks at the centre is obtained. For higher values of St^+ the turbophoretic effect, expressed mathematically by (2.9), becomes more important. The shape of $\bar{c}(r)$ is determined by the competing effects of turbophoresis (that accumulates particles close to the wall leading to sharper profiles) and turbulent diffusion (that smooths out the
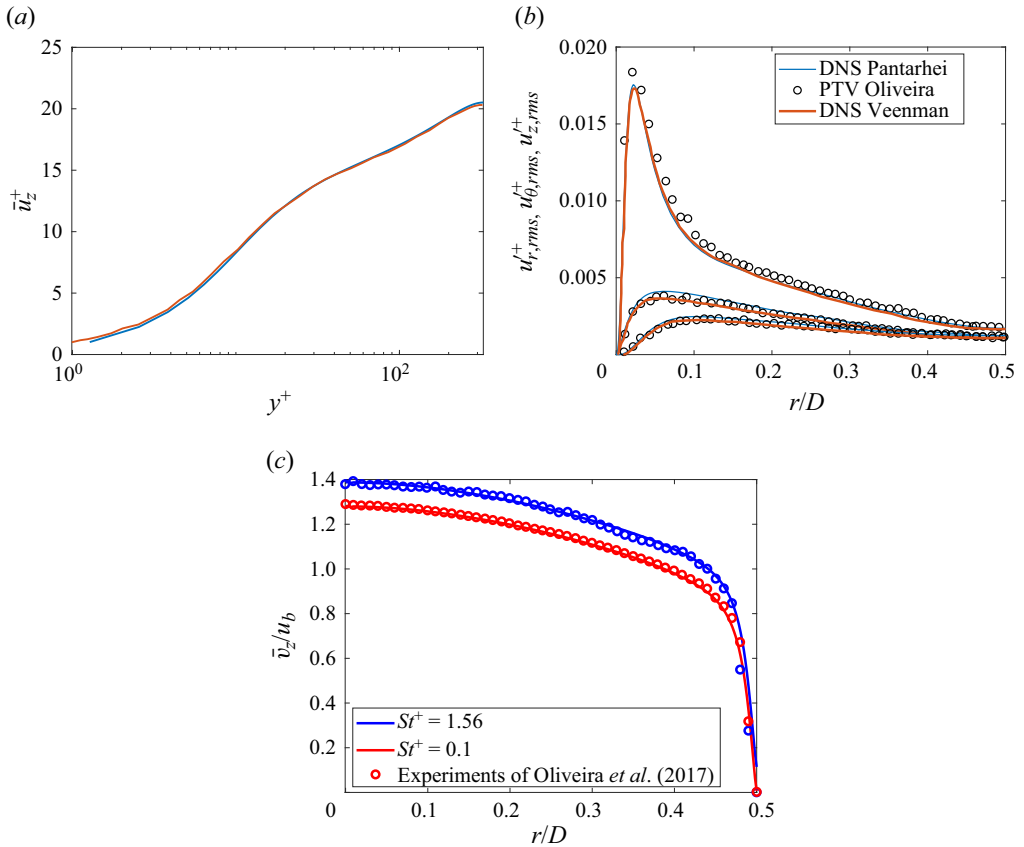
Figure 1. Comparison of radial profiles of mean streamwise velocity (*a*) and $u'_{r,rms}$, $u'_{\theta,rms}$, $u'_{z,rms}$ (*b*) against results from the literature for pipe flow at $Re = 10\,300$. In (*c*) the mean streamwise particle velocity $\bar{v}_z$ is compared with the experiments of Oliveira *et al.* (2017) for downward flow.

profiles). Lagrangian simulations with particles that elastically rebound from the wall show that, for $St^+ = 10 - 50$, turbophoresis results in very sharp increase of $\bar{c}$ close to the wall with respect to the centreline, but for $St^+ = 1$ this effect is much weaker; see for example Sardina *et al.* (2012). Simulations with particle deposition, i.e. absorbing walls, are much more rare in the literature. For $St^+ = 3$, the Eulerian deposition model of Young & Leeming (1997) matches approximately the Lagrangian results of Brooke, Hanratty & McLaughlin (1994) with absorbing wall; $\bar{c}$ peaks at $y^+ \approx 1$ and is approximately 8–10 times larger compared with $y^+ = 40$. It is expected that, for $St^+ = 1$, the profile will be much smoother (compare for example the profiles for $St^+ = 1$ and $St^+ = 5$ in figure 7 of Sardina *et al.* 2012). We use the profile of $St^+ = 1$ in the resolvent analysis in the § 5. In order to examine the sensitivity of the results to $\bar{c}(r)$, we also employ the concentration profile of Sardina *et al.* (2011) that was obtained from Lagrangian simulations in pipe flow.

The r.m.s. profiles plotted in figure 3(*b*) show that the r.m.s. values increase with St^+, the increase being more prominent for the two largest St^+ considered. For $Fr = \pm 4$, gravity does not seem to affect significantly the mean and r.m.s. profiles. The effect of gravity becomes more important for $Fr_z = \pm 0.4$, see figures 3(*c*) and 3(*d*). As St^+ increases, the
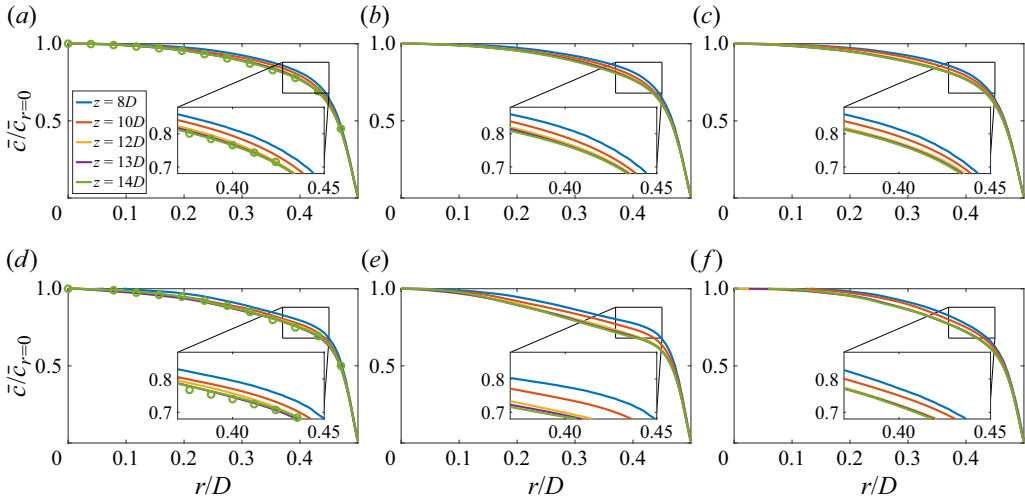
985 A27-8

Figure 2. Radial concentration profiles at different streamwise locations for $St^+ = 0.1$ top row (a–c) and $St^+ = 1$ bottom row (d–f). The left column (a,d) shows results without gravity, the middle column (b,e) results for $Fr_z = 0.4$, and the right column (c,f) for $Fr_z = -0.4$. Circles (o) in the no-gravity plots (left column) denote results from the DNS simulation in the larger domain, $L = 15D$.
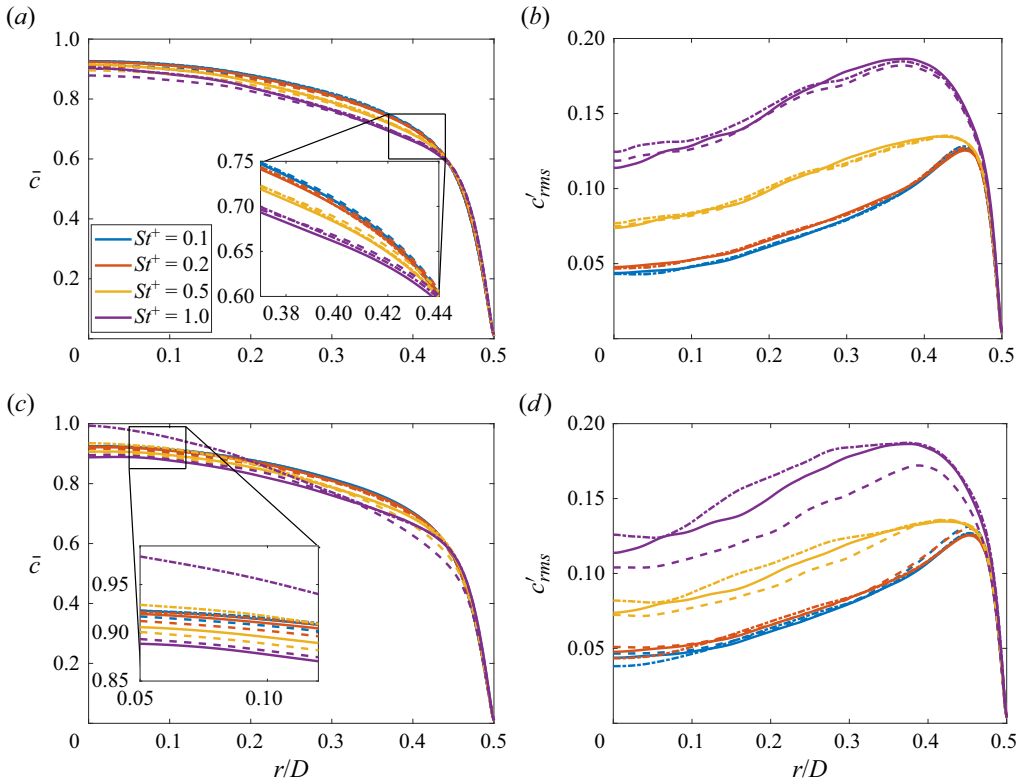

Figure 3. Mean particle concentration profiles at $z = 14D$ are shown in (a) and (c), and r.m.s. profiles are shown in (b) and (d), for $St^+ = 0.1 - 1$. Solid lines denote no-gravity, (- -) upward flow and (-.-) downward flow. Top row panels (a) and (b) are for $Fr_z = \pm 4$, and bottom row panels (c) and (d) for $Fr_z = \pm 0.4$.

concentration also increases in the pipe's centre for downward flows (dash-dotted line), in agreement with Nilsen *et al.* (2013) and Uijttewaal & Oliemans (1996).

5. Resolvent operator of turbulent flow laden with low-inertia particles

5.1. *Derivation of the resolvent operator*

Due to particle deposition at the wall, the section-average (or bulk) particle concentration, defined as $\bar{c}_B(z) = 8\int_0^{1/2} \bar{u}_z \bar{c} r \, dr$, decreases in the streamwise direction, as shown in figure 4. It can be shown analytically that, for a scalar, i.e. for $St^+ = 0$, $\bar{c}_B(z)$ decays exponentially $\bar{c}_B(z) \sim e^{-az}$; see Incropera *et al.* (2007) and Schlander *et al.* (2022). Figure 4 shows this is also true for the range of St^+ and Fr considered in this paper, but with slightly different values of the decay rate a. Since the normalised particle concentration profiles $\bar{c}(r,z)/\bar{c}_{r=0}(z)$ become self-similar after a development distance (as shown in figure 2), so does $\bar{c}(r,z)/\bar{c}_B(z)$. We define the scaled particle concentration as

$$c_h(r,z,t) = \frac{\bar{c}_w - c(r,z,t)}{\bar{c}_w - \bar{c}_B(z)} = \frac{c(r,z,t)}{\bar{c}_B(z)}, \tag{5.1}$$

because $c_w = \bar{c}_w = 0$, and the subscript 'h' stands for homogeneous, because $\bar{c}_h(r)$ is independent of z. We can now rewrite equation (2.7) in terms of $c_h(r,z,t)$ using transformation (5.1). The resulting expression in polar coordinates is

$$\frac{\partial c_h}{\partial t} + \frac{1}{r}\frac{\partial(rv_r c_h)}{\partial r} + \frac{1}{r}\frac{\partial(v_\theta c_h)}{\partial \theta}$$
$$+ \frac{\partial(v_z c_h)}{\partial z} = \frac{1}{ReSc}\left[\frac{1}{r}\frac{\partial}{\partial r}\left(r\frac{\partial c_h}{\partial r}\right) + \frac{1}{r^2}\frac{\partial^2 c_h}{\partial \theta^2} + \frac{\partial^2 c_h}{\partial z^2}\right] + S_{c_h}, \tag{5.2}$$

where

$$S_{c_h} = av_z c_h + \frac{1}{ReSc}\left(-2a\frac{\partial c_h}{\partial z} + a^2 c_h\right), \tag{5.3}$$

is the source term arising from the exponential decay of $\bar{c}_B(z)$. The corresponding equation for passive scalar, where $v_i = u_i$, appears in Straub *et al.* (2019). The governing equations are therefore (2.1) and (5.2), with the flow and scalar quantities being homogeneous in the streamwise direction, and expression (2.5) relating particle and fluid velocities. We are ready now to proceed with the derivation of the resolvent operator.

Applying Fourier transform, the vector $\boldsymbol{q} = [\boldsymbol{u}', p', c_h']^\top$, that comprises the instantaneous fluctuations of the velocity $\boldsymbol{u}' = [u_z', u_r', u_\theta']^\top$, pressure and particle concentration fields, can be written as

$$\boldsymbol{q}'(r,\theta,z,t) = \begin{bmatrix} \boldsymbol{u}'(r,\theta,z,t) \\ p'(r,\theta,z,t) \\ c_h'(r,\theta,z,t) \end{bmatrix}$$
$$= \sum_{k_\theta=-\infty}^{+\infty}\int_{-\infty}^{\infty}\int_{-\infty}^{\infty}\begin{bmatrix} \hat{\boldsymbol{u}}(r;k_z,k_\theta,\omega) \\ \hat{p}(r;k_z,k_\theta,\omega) \\ \hat{c}_h(r;k_z,k_\theta,\omega) \end{bmatrix} e^{i(k_z z + k_\theta\theta - \omega t)}\, dk_z\, d\omega, \tag{5.4}$$

where k_z is the streamwise wavenumber, k_θ is the azimuthal wavenumber (constrained to be an integer), ω is the angular frequency and the caret ˆ symbol denotes a
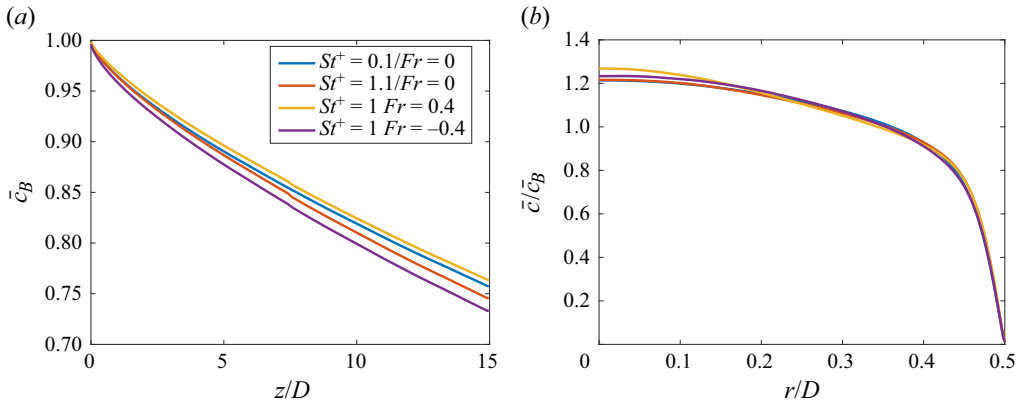
985 A27-10

Figure 4. Bulk concentration $\bar{c}_B(z)$ along the streamwise direction (*a*) and scaled concentration profiles $\bar{c}_h(r) = \bar{c}/\bar{c}_B$ (*b*) for $St^+ = 0, 1$ and $1/Fr = 0, Fr = \pm 0.4$.

Fourier-transformed variable. This Fourier decomposition leads to the wavenumber–frequency vector $\boldsymbol{k} = (k_z, k_\theta, c_w = \omega/k_z)$, which represents a rotating helical wave propagating downstream with wave speed, c_w, for $\boldsymbol{k} \neq (0, 0, 0)$. Wavelengths in the θ and z directions are defined as $\lambda_\theta = 2R\pi/k_\theta$ and $\lambda_z = 2\pi/k_z$, respectively. At the critical layer, located at y_v, the wave speed, c_w, is equal to the mean streamwise velocity, $c_w = \bar{u}(y_v)$.

Using this Fourier representation, at each wavenumber–frequency vector, $\boldsymbol{k}$, the Navier–Stokes and particle concentration equations can be written as

$$(-\mathrm{i}\omega + \mathrm{i}k_z\bar{u}_z)\hat{\boldsymbol{u}} + \hat{u}_r\frac{\partial\bar{u}_z}{\partial r}\boldsymbol{e}_z + \boldsymbol{\nabla}\hat{p} - Re^{-1}\Delta\hat{\boldsymbol{u}} = \hat{\boldsymbol{f}}_u, \tag{5.5}$$

$$\mathrm{i}k_z\hat{u}_z + \frac{\hat{u}_r}{r} + \frac{\partial\hat{u}_r}{\partial r} + \frac{\mathrm{i}k_\theta\hat{u}_\theta}{r} = 0, \tag{5.6}$$

$$(-\mathrm{i}\omega + \mathrm{i}k_z\bar{u}_z)\hat{c}_h + \hat{u}_r\frac{\partial\bar{c}_h}{\partial r} + St\left(\mathrm{i}\omega\hat{u}_r\frac{\partial\bar{c}_h}{\partial r} - 2\,\mathrm{i}k_z\hat{u}_r\frac{\partial\bar{u}_z}{\partial r}\bar{c}_h - \mathrm{i}k_z\hat{u}_r\bar{u}_z\frac{\partial\bar{c}_h}{\partial r}\right)$$

$$+ \frac{St}{Fr_z}\mathrm{i}k_z\hat{c}_h - Re^{-1}Sc^{-1}\Delta\hat{c}_h - [\Theta_{s,z}(\hat{u}_z) + \Theta_{s,r}(\hat{u}_r) + \Theta_{s,c}(\hat{c}_h)] = \hat{f}_c, \tag{5.7}$$

where

$$\boldsymbol{\nabla} = \begin{bmatrix} \mathrm{i}k_z \\ \dfrac{\partial}{\partial r} \\ \dfrac{\mathrm{i}k_\theta}{r} \end{bmatrix}, \tag{5.8}$$

$$\Delta = -k_z^2 - (k_\theta^2 + 1)r^{-2} + \frac{\partial^2}{\partial r^2} + r^{-1}\frac{\partial}{\partial r}, \tag{5.9}$$

are the gradient and Laplacian operators in polar coordinates respectively, and $\boldsymbol{e}_z$ is the unit vector in the streamwise direction. See Appendix A for the derivation of (5.7) and the definition of the linear operators $\Theta_{s,z}$, $\Theta_{s,r}$ and $\Theta_{s,c}$. Nonlinear terms are included in the forcings $\boldsymbol{f_u} = -\boldsymbol{u}' \cdot \boldsymbol{\nabla}\boldsymbol{u}' + \overline{\boldsymbol{u}' \cdot \boldsymbol{\nabla}\boldsymbol{u}'}$ and $f_c = -\boldsymbol{\nabla} \cdot (\boldsymbol{v}'c_h') + \overline{\boldsymbol{\nabla} \cdot (\boldsymbol{v}'c_h')}$ and define the forcing vector $\hat{\boldsymbol{f}} = [\hat{\boldsymbol{f}}_u, \hat{f}_c]^\top$ in Fourier domain.

Equations (5.5)–(5.7) represent a forcing–response relationship that can be put in matrix form as

$$
\left(
-\mathrm{i}\omega
\underbrace{
\begin{bmatrix}
\boldsymbol{I} & & \\
 & 0 & \\
 & & I
\end{bmatrix}
}_{\boldsymbol{I}_{\boldsymbol{u},c_h}}
+
\underbrace{
\begin{bmatrix}
\boldsymbol{L_u} & \nabla & 0 \\
\nabla^\top & 0 & 0 \\
L_{\boldsymbol{u},c} & 0 & L_c
\end{bmatrix}
}_{\boldsymbol{L}}
\right)
\begin{bmatrix}
\hat{\boldsymbol{u}} \\
\hat{p} \\
\hat{c}_h
\end{bmatrix}
=
\underbrace{
\begin{bmatrix}
\boldsymbol{I} & 0 \\
0 & 0 \\
0 & I
\end{bmatrix}
}_{\boldsymbol{B}}
\underbrace{
\begin{bmatrix}
\hat{\boldsymbol{f}}_u \\
\hat{f}_c
\end{bmatrix}
}_{\hat{f}},
\tag{5.10}
$$

where $\boldsymbol{L_u}$ is the linear Navier–Stokes operator, $[L_{\boldsymbol{u},c}\ 0\ L_c]$ is the linear particle transport operator and $\boldsymbol{I}$ and I are identity matrices of similar size as $\hat{\boldsymbol{u}}$ and $\hat{c}_h$, respectively. Matrix $\boldsymbol{B}$ is inserted to account for the fact that there is no forcing term in the continuity equation. The expanded form of operator $-\mathrm{i}\omega\boldsymbol{I}_{\boldsymbol{u},c_h} + \boldsymbol{L}$ in polar coordinates is given below

$$
-\mathrm{i}\omega\boldsymbol{I}_{\boldsymbol{u},c_h} + \boldsymbol{L} =
\begin{bmatrix}
-\mathrm{i}\omega + A - \dfrac{r^{-2}}{Re} & \dfrac{\partial \bar{u}_z}{\partial r} & 0 & \mathrm{i}k_z & 0 \\[2mm]
0 & -\mathrm{i}\omega + A & \dfrac{2\mathrm{i}k_\theta r^{-2}}{Re} & \dfrac{\partial}{\partial r} & 0 \\[2mm]
0 & -\dfrac{2\mathrm{i}k_\theta r^{-2}}{Re} & -\mathrm{i}\omega + A & r^{-1}\mathrm{i}k_\theta & 0 \\[2mm]
\mathrm{i}k_z & r^{-1} + \dfrac{\partial}{\partial r} & \mathrm{i}r^{-1}k_\theta & 0 & 0 \\[2mm]
A_{c_1} & A_{c_2} & 0 & 0 & -\mathrm{i}\omega + A_{c_5}
\end{bmatrix},
\tag{5.11}
$$

where

$$
A = \mathrm{i}k_z\bar{u}_z - \frac{\Delta}{Re},
\tag{5.12}
$$

$$
A_{c_1} = -\Theta_{s,z},
\tag{5.13}
$$

$$
A_{c_2} = \frac{\partial \bar{c}_h}{\partial r} + St\left(\mathrm{i}\omega\frac{\partial \bar{c}_h}{\partial r} - 2\mathrm{i}k_z\frac{\partial \bar{u}_z}{\partial r}\bar{c}_h - \mathrm{i}k_z\bar{u}_z\frac{\partial \bar{c}_h}{\partial r}\right) - \Theta_{s,r},
\tag{5.14}
$$

and

$$
A_{c_5} = \mathrm{i}k_z\bar{u}_z - \frac{\Delta}{ReSc} + \mathrm{i}k_z\frac{St}{Fr_z} - \Theta_{s,c}.
\tag{5.15}
$$

Inverting equation (5.10) we get,

$$
\hat{q} \equiv
\begin{bmatrix}
\hat{\boldsymbol{u}} \\
\hat{p} \\
\hat{c}_h
\end{bmatrix}
= \boldsymbol{H}\hat{f},
\tag{5.16}
$$

where

$$
\boldsymbol{H} = (-\mathrm{i}\omega\boldsymbol{I}_{\boldsymbol{u},c_h} + \boldsymbol{L})^{-1}\boldsymbol{B},
\tag{5.17}
$$

is the resolvent operator.

We define the energy norm

$$
2E = \int_0^{1/2} (\alpha\hat{\boldsymbol{u}}^*\hat{\boldsymbol{u}} + \beta\hat{c}_h^*\hat{c}_h)r\,\mathrm{d}r,
\tag{5.18}
$$

where α and β are the weights of the velocity and particle concentration fields, respectively, and the asterisk $()^*$ denotes complex conjugate. A similar norm was

985 A27-12

previously analysed in Dawson, McKeon & Saxton-Fox (2018) for a passive scalar. For $\beta = 0$, we obtain the standard kinetic energy norm and for $\alpha = 0$ the concentration variance norm. It must be noted that, if we set either α or β equal to zero, we obtain a seminorm instead of a standard norm, meaning that the uniqueness property, $\|q\| = 0$, implies $q = 0$, is not satisfied. However, it was shown in Dawson & McKeon (2020), that using a seminorm in the case of a compressible channel flow, did not affect the response mode shapes.

The objective now is to compute the forcing $\hat{f}$ that will maximise the norm E for each wavenumber–frequency vector k. To this end, we apply SVD to the discrete form of an appropriately scaled resolvent operator. More specifically, the operator is discretised in the radial direction using a Chebyshev pseudospectral method; see details in § 5.2 below. The discrete form of the energy norm E can be written as $E = (W_q B^\top \hat{q})^\top (W_q B^\top \hat{q})$ and the energy of the forcing as $E_f = (W_f \hat{f})^\top (W_f \hat{f})$, where matrices W_q and W_f are defined as,

$$
W_q = \begin{bmatrix} \sqrt{\alpha} W_r & & & \\ & \sqrt{\alpha} W_r & & \\ & & \sqrt{\alpha} W_r & \\ & & & \sqrt{\beta} W_r \end{bmatrix}, \quad W_f = \begin{bmatrix} W_r & & & \\ & W_r & & \\ & & W_r & \\ & & & W_r \end{bmatrix},
$$

(5.19a,b)

where W_r is the weighting due to numerical quadrature. Multiplying (5.16) from the left with $W_q B^\top$ we get

$$
W_q B^\top \hat{q} = (W_q B^\top H W_f^{-1})(W_f \hat{f}) = H_S(W_f \hat{f}),
$$

(5.20)

where $H_S = W_q B^\top H W_f^{-1}$ is the scaled resolvent operator. Applying standard SVD to H_S will provide the forcing and the response $\hat{q}$ that will maximise the energy norm E. Therefore we obtain the following SVD decomposition of H_S:

$$
H_S = \sum_j \sigma_j(k) \hat{\psi}_{S,j}(r; k) \hat{\phi}_{S,j}^*(r; k),
$$

(5.21)

where ϕ_S and ψ_S are the weighted forcing and response modes (with W_f and W_q, respectively) and σ is the gain. These modes are orthonormal

$$
\hat{\phi}_{S,i}^* \hat{\phi}_{S,j} = \hat{\psi}_{S,i}^* \hat{\psi}_{S,j} = \delta_{ij},
$$

(5.22)

as per standard SVD. The true forcing mode is

$$
\hat{\phi}_i = W_f^{-1} \hat{\phi}_{S,i},
$$

(5.23)

which we use together with the unscaled resolvent operator to find the unscaled response modes

$$
\sigma_i \hat{\psi}_i = H \hat{\phi}_i.
$$

(5.24)

These modes satisfy the orthogonality condition

$$
\langle \hat{\phi}_i, \hat{\phi}_j \rangle \equiv \hat{\phi}_i^* W_q^2 \hat{\phi}_j = \delta_{ij}, \quad \langle \hat{\psi}_i, \hat{\psi}_j \rangle \equiv \hat{\psi}_i^* W_f^2 \hat{\psi}_j = \delta_{ij}.
$$

(5.25a,b)

The above equation serves also as the definition of the inner product (denoted by angular brackets) between two response or between two forcing vectors. The actual forcing and

response can be projected into the corresponding modes

$$\hat{f}(r; \boldsymbol{k}) = \sum_{j=1} \chi_j(\boldsymbol{k}) \hat{\boldsymbol{\phi}}_j(r; \boldsymbol{k}), \tag{5.26}$$

$$\hat{q}(r; \boldsymbol{k}) = \sum_{j=1} \chi_j(\boldsymbol{k}) \sigma_j(\boldsymbol{k}) \hat{\boldsymbol{\psi}}_j(r; \boldsymbol{k}), \tag{5.27}$$

where $\chi_j(\boldsymbol{k})$ is the projection coefficient given by

$$\chi_j(\boldsymbol{k}) = \langle \hat{f}, \hat{\boldsymbol{\phi}}_j \rangle. \tag{5.28}$$

The forcing shape that gives the largest norm is $\hat{f}(r; \boldsymbol{k}) = \hat{\boldsymbol{\phi}}_1(r; \boldsymbol{k})$, i.e. when it is aligned with the principal singular vector. The resolvent operator is low rank when $\sigma_1 \gg \sigma_2$. In §6.1 we study the principal forcing ϕ_1, the response modes ψ_1, and the singular values σ_1 for different vectors $\boldsymbol{k}$.

Using the operators (5.13)–(5.15), the particle concentration equation (5.7) can be written in compact form as (see also (A11))

$$A_{c_1} \hat{u}_z + A_{c_2} \hat{u}_r + (-\mathrm{i}\omega + A_{c_5}) \hat{c}_h = \hat{f}_c, \tag{5.29}$$

from which

$$\begin{aligned} \hat{c}_h &= (-\mathrm{i}\omega + A_{c_5})^{-1} (\hat{f}_c - A_{c_1} \hat{u}_z - A_{c_2} \hat{u}_r) \\ &= (-\mathrm{i}\omega + A_{c_5})^{-1} \hat{f}_c - (-\mathrm{i}\omega + A_{c_5})^{-1} (A_{c_1} \hat{u}_z + A_{c_2} \hat{u}_r). \end{aligned} \tag{5.30}$$

The first term on the right-hand side depends on the nonlinear forcing, but the second term

$$\tilde{\hat{c}}_h = -(-\mathrm{i}\omega + A_{c_5})^{-1} (A_{c_1} \hat{u}_z + A_{c_2} \hat{u}_r), \tag{5.31}$$

can be computed directly from the velocity modes, see also Dawson *et al.* (2018) who applied this for passive scalars.

Furthermore, we can treat the weighted $(-\mathrm{i}\omega + A_{c_5})^{-1}$ as a simplified resolvent operator

$$Q_w = (W_r)(-\mathrm{i}\omega + A_{c_5})^{-1}(W_r^{-1}) = \sum_{j=1} \sigma_{Q,j}(\boldsymbol{k}) \hat{\boldsymbol{\psi}}_{Q,j}(r; \boldsymbol{k}) \hat{\boldsymbol{\phi}}_{Q,j}^*(r; \boldsymbol{k}). \tag{5.32}$$

It is interesting to note that this operator is independent of the time-average particle concentration profile $\bar{c}_h(r)$, only the velocity profile $\bar{u}_z(r)$ is required. We show later that some features of the full resolvent operator are captured by the simplified form (5.32).

We close this sub-section by making an important observation that will prove useful later. It is possible to define two critical layers, one for the velocity field, y_v, where

$$c_w = \bar{u}_z(y_v), \tag{5.33}$$

and one for the particle concentration field, y_c, where

$$c_w = \bar{u}_z(y_c) + \frac{St}{Fr_z}. \tag{5.34}$$

The first is well known, but to the best of our knowledge the second is new, and appears because gravity is acting in the streamwise direction. The motivation to define y_c in this

way originates from the diagonal element $-\mathrm{i}\omega + A_{c_5}$, that can be written as

$$-\mathrm{i}\omega + A_{c_5} = -\mathrm{i}\omega + \mathrm{i}k_z\bar{u}_z - \frac{\Delta}{ReSc} + \mathrm{i}k_z\frac{St}{Fr_z} - \Theta_{s,c} = \mathrm{i}k_z\left(-c_w + \bar{u}_z + \frac{St}{Fr_z}\right)$$
$$- \frac{\Delta}{ReSc} - \Theta_{s,c}. \tag{5.35}$$

The term St/Fr_z encapsulates the combined effects of inertia and gravity and vanishes when considering a standard scalar ($St = 0$) or when gravity is absent ($1/Fr_z = 0$). Using (5.34) leads to $-\mathrm{i}\omega + A_{c_5} = -\Delta/ReSc - \Theta_{s,c}$, with the first term tending to 0 as Re grows, leaving only the term related to the streamwise decay. Therefore for the locations and frequencies for which (5.34) is satisfied, large response is expected.

5.2. *Computational details*

The discrete form of the resolvent operator is constructed using Chebyshev differentiation matrices. The radial profiles of the time-average velocity and particle concentration are interpolated onto the Chebyshev collocation points. At the wall, we implement a no-slip condition for velocities and a totally absorbing wall for the particle concentration, i.e. $\hat{c}_h(R) = 0$.

The discrete operator has a block structure, as seen in (5.10), and each block has dimensions $N_r \times N_r$ (where N_r is the grid resolution), thus L has size $5N_r \times 5N_r$. Based on the work of Jane Bae, Dawson & McKeon (2019) and Ahmed *et al.* (2021) among others, as well as a grid convergence study, we have selected $N_r = 256$. The numerical implementation is an extension to that of Luhar *et al.* (2014). For each wavenumber–frequency vector, k the SVD of H_S can be computed within a few seconds at most on a personal computer. The discrete form of the energy norm is obtained using numerical quadrature; see Trefethen (2000) for more details on the numerical computation of resolvent modes.

6. Results and discussion

In this section, we apply the resolvent framework to investigate the interaction between turbulent flow and particle concentration fluctuations for different Stokes and Froude numbers. First, we study the resolvent spectra and then analyse the mode shapes and investigate inertial clustering and near-wall accumulation through the lens of the resolvent operator. In following, we assume unit broadband forcing, i.e. $\chi_j(k) = 1$ in (5.26), and therefore omit the analysis of the actual forcing; we acknowledge, however, that it is an interesting research topic; see for example Morra *et al.* (2021) for single-phase flows.

6.1. *Resolvent spectra*

The resolvent gains, $\sigma_j(k)$, provide information about how the system reacts to forcing; see (5.27). The larger the principal gain $\sigma_1(k)$ is with respect to the rest, the more sensitive the system is to forcing in the $\hat{\phi}_1(k)$ direction. A system is said to have low rank if a significant fraction of the total response is captured by the response to a few dominant forcing modes, in the limiting case just one forcing mode. In the latter case, $H_S(k) \approx \sigma_1(k)\hat{\psi}_1(k)\hat{\phi}_1^*(k)$, and the actual response $\hat{q}(r; k)$ in (5.27) is dominated by the first term, $\chi_1(k)\sigma_1(k)\hat{\psi}_1(r; k)$ (provided that the actual forcing has appreciable component in the $\hat{\phi}_1(r; k)$ direction, thus the large $\sigma_1(k)$ is not compensated by a low $\chi_1(k)$).

In this context, we investigate the ratio $\sigma_1^2 / \sum_{j=1,5N_r} \sigma_j^2$ with respect to St^+ and Fr for different $\boldsymbol{k}$. Recall that the energy of the response for unit broadband forcing, i.e. for $\chi_j(\boldsymbol{k}) = 1$, is equal to $\sum_{j=1,5N_r} \sigma_j^2$; see McKeon & Sharma (2010). Therefore this ratio represents the energy of the leading response mode relative to the total energy of the response; a value close to 1 indicates low-rank behaviour.

First, we study the effect of the choice of the energy norm (5.18) on the energy gain ratio for wave speed $c_w = \bar{u}(y_v^+ = 15)$ and various streamwise and azimuthal wavenumbers. When $c_w = \bar{u}(y_v)$, that is at the critical layer of the velocity field, the diagonal terms of the operator $(-i\omega I + L_u)$ become very small, resulting in a large response for a given input. We select in particular $y_v^+ = 15$, because it corresponds to the location of the peak activity of the near-wall cycle. The results are shown in figure 5 for the no-gravity case ($1/Fr_z = 0$), with $St^+ = 0$ (no inertia, panels a-d) and $St^+ = 1$ (panels e-h). In this case, the velocity and particle critical layers are in the same location.

For $\alpha = 1, \beta = 0$, figure 5(*a,e*), the ratio is independent of St since only the Navier–Stokes equations are considered and there is only one-way coupling, thus the presence of the particles does not affect the flow. The low-rank zone (dark red area) is around $\lambda_\theta^+ > 10$ and $\lambda_z^+ > 100$ with a local peak at $\lambda_\theta^+ \approx 100$, $\lambda_z^+ \approx 1000$, which corresponds to the well-known length scales of the near-wall streaks. The gain plots of the present analysis are qualitatively similar to the plots of Moarref *et al.* (2013) and Ahmed *et al.* (2021), but the latter were obtained for channel flow.

The effect of inertia can be seen by setting $\alpha = 0, \beta = 1$. Comparing figures 5(*b*) and 5(*f*) that depict results for $St^+ = 0$ and $St^+ = 1$, respectively, it can be seen that increasing St increases the energy gain ratio for the smallest streamwise wavelengths (notice the shift to the left), which means that low-rank behaviour appears at smaller length scales for the particle concentration compared with the flow. The shift appears only in the streamwise direction; in the azimuthal direction, there is no change. This behaviour can be (partially) explained by inspecting equation (5.7); the terms involving the Stokes number contain only k_z, not k_θ. In figures 5(*c*) and 5(*g*) the energy gain ratio is shown for $\alpha = 1, \beta = 1$; and the plots show features from both of the previous sets of plots with $\alpha = 1, \beta = 0$ and $\alpha = 0, \beta = 1$.

The fact that low-rank behaviour appears for smaller λ_z for particles is consistent with the existence of local particle clustering; see Maxey (1987), Squires & Eaton (1991), Marchioli *et al.* (2007), Sardina *et al.* (2012) and Brandt & Coletti (2022), among many others. Contour plots of instantaneous particle concentrations for 3 Stokes numbers are shown in figure 6. The different particle concentration fields are simulated simultaneously with the same flow field, which makes it easier to elucidate the effect of inertia. Increasing the Stokes number indeed results in more compact regions of high particle concentration and regions almost void of particles, consistent with the aforementioned literature and the results of the resolvent analysis. Consider for example the same rectangular area marked with a black boundary in the three plots. The vortex structures are the same for all Stokes numbers, however, the particle concentration fields are different; they are much more localised for $St^+ = 1$ compared with the other 2 values.

Returning to figure 5, in all plots, line contours of the pre-multiplied velocity, $E_{uu} = k_z k_\theta \hat{u}_z^* \hat{u}_z$, or particle concentration fluctuation spectra, $E_{cc} = k_z k_\theta \hat{c}_h^* \hat{c}_h$, obtained from the corresponding DNS are superimposed. The spectra have been calculated from 600 snapshots of the concentration field, interpolated onto a structured cylindrical grid with $(N_r, N_\theta, N_z) = (256, 128, 256)$ data points. The overall trend of the pre-multiplied spectra is captured by the resolvent analysis, with the locations of the peaks being nearly identical. Furthermore, the pre-multiplied spectra of c_h shift to the left, i.e. towards smaller
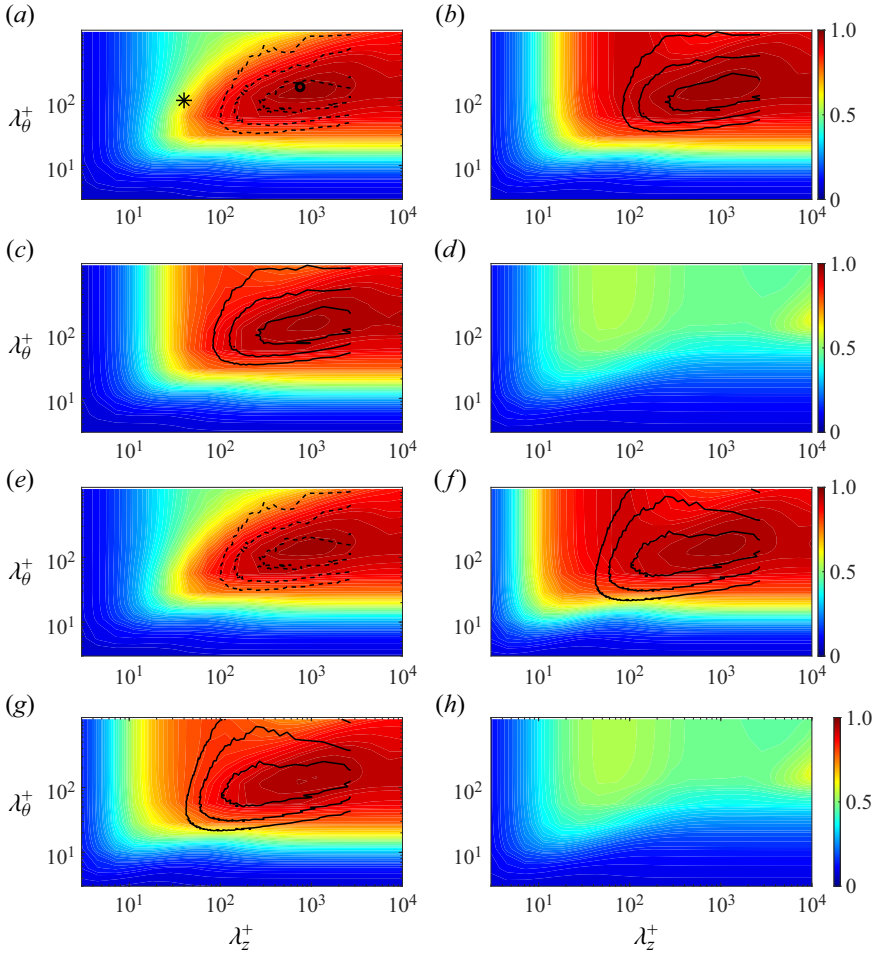
Figure 5. Contour plots of the energy gain ratio $\sigma_1^2 / \sum_{j=1,5N_r} \sigma_j^2$ for $c_w = \bar{u}_z(y_v^+ = 15)$ for the no-gravity case, $1/Fr_z = 0$. In (a,e) the norm is the kinetic energy of the velocity fluctuations, $\alpha = 1$, $\beta = 0$, in (b,f) the norm is the particle concentration variance, $\alpha = 0$, $\beta = 1$, in (c,g) a combined norm is considered with $\alpha = 1$, $\beta = 1$ and in (d,h), the energy gain ratio of the simplified resolvent operator from (5.32) is shown. The Stokes number is $St^+ = 0$ in panels $(a–d)$ and $St^+ = 1.0$ in panels $(e–h)$. The pre-multiplied spectra, $E_{uu} = k_z k_\theta \hat{u}_z^* \hat{u}_z$ (dashed lines) and $E_{cc} = k_z k_\theta \hat{c}_h^* \hat{c}_h$ (solid lines) from the DNS are superimposed on the resolvent gain plots. The contour lines represent 75 %, 50 % and 10 % of the maximum energy in the spectrum. In panel (a), an open circle indicates the wavelengths of a representative mode and the star the wavelengths of a locally clustered mode; the modes are analysed in § 6.2.

wavelengths, that is, energy is increased for smaller structures. This is in agreement with the contour plots of particle concentration of figure 6 and the prediction of resolvent analysis.

Direct comparison of the present results with concentration spectra from Lagrangian simulations is difficult. The main reason is the sensitivity to the bin size when computing Eulerian statistics from discrete particle positions; see Sardina *et al.* (2011) for details. On the other hand, Voronoi analysis of preferential particle concentration is much more robust, because it does not require the selection of an arbitrary length scale; see Monchaux, Bourgoin & Cartellier (2010) and Tagawa *et al.* (2012). The idea is to divide the computational domain into subvolumes, each consisting of all points that
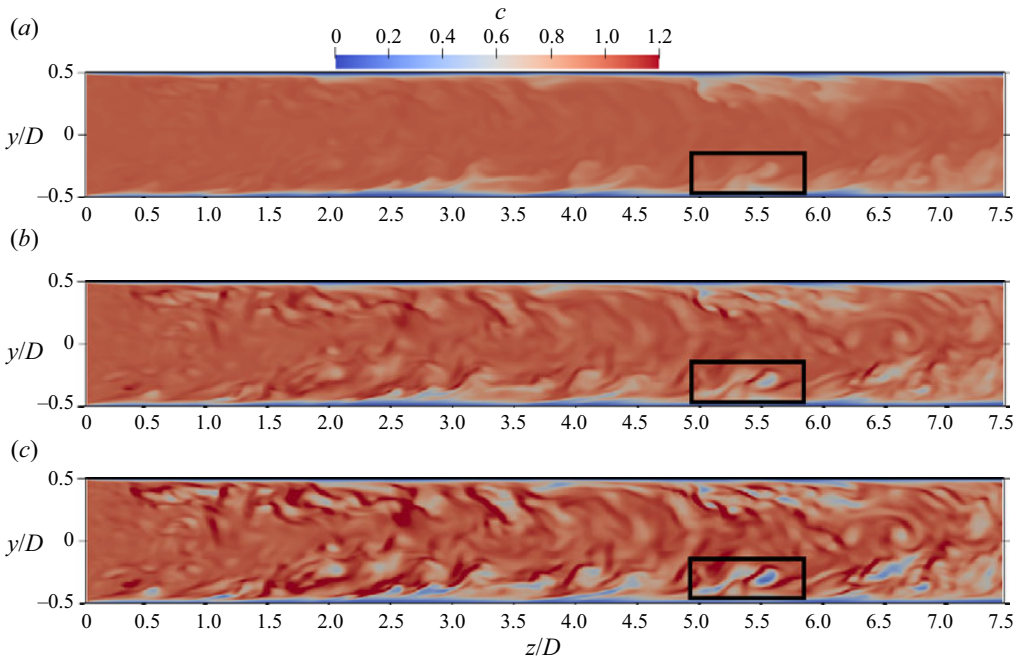
Figure 6. Instantaneous contours of particle concentrations for $Re = 5300$ for $St^+ = 0$ (*a*), $St^+ = 0.5$ (*b*) and $St^+ = 1.0$ (*c*) for the no-gravity case, $1/Fr_z = 0$. The background flow is identical for the three Stokes numbers. To facilitate comparison, a thick black line marks the boundary of the same rectangular area in the three plots.

are closer to one particular particle compared with all other particles. This results in a specific particle volume (or inverse particle number density) that can be further analysed. Particle clustering can be quantified from the probability density function (PDF) of the normalised volumes (or areas in two-dimensional problems) of the Voronoi cells. Such PDFs, computed at different wall-normal locations inside a channel, are shown in figure 5 of Nilsen *et al.* (2013). The results clearly show higher probability for low specific particle volumes, i.e. high particle number density, indicative of particle clustering. Unfortunately, we could not find in the literature spectra of the normalised volumes of Voronoi cells in the $(\lambda_z^+, \lambda_\theta^+)$ plane to compare against our results.

The energy gain ratio from the SVD of the simplified resolvent operator Q_w in (5.32) is shown in figure 5(*d,h*). The results shown in the two panels are identical because (5.32) is independent of Stokes number when gravity is ignored. The extent of the region of low-rank behaviour is captured but it is much more diffuse and the gain ratio does not exceed approximately 0.6. This indicates that to get accurate results that match with DNS spectra, the full operator must be considered. This makes physical sense; without the effect of the fluctuating velocity field, it is not possible to reproduce correct concentration spectra.

Next, the effect of gravity is examined. We start by keeping only the term multiplied with St/Fr_z in (5.7) and (only temporarily) neglect the term multiplied with St. This removes the influence of inertia but retains gravitational effects, thus the model becomes equivalent to the dusty gas model; see Carrier (1958) and Marble (1970). The energy gain ratio for this model is plotted in the first row of figure 7 for $St/|Fr| = 0.1$, corresponding to the combination $St^+ = 1(St = 0.04)$ and $Fr = \pm0.4$. The frequency is selected to satisfy $c_w = \bar{u}(y_v^+ = 15)$. The results for the downward flow, figure 7(*a*) are similar to those without
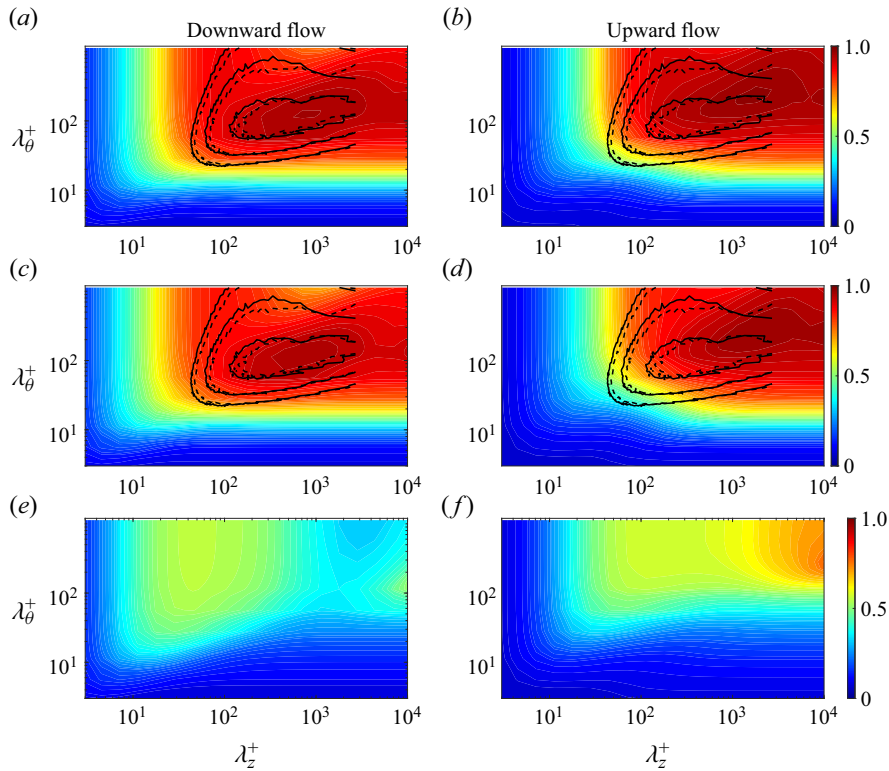
Figure 7. Contour plots of the energy gain ratio $\sigma_1^2 / \sum_{j=1,5N_r} \sigma_j^2$ for $c_w = \bar{u}_z(y_v^+ = 15)$ with gravity included in the resolvent operator. In the first row (a,b) the term multiplied with St/Fr_z is retained in (5.7), but the term multiplied with just St is neglected (this assumption corresponds to the dusty gas model). In the middle row (c,d) all terms are retained. In the bottom row (e,f), the energy gain ratio of the simplified equation (5.32) is shown. Panels (a,c,e) on the left column depict a downward flow with $St/Fr_z = 0.1$ and panels (b,d,f) on the right column an upward flow with $St/Fr_z = -0.1$. The energy norm is the same for all plots with $\alpha = 0$, $\beta = 1$. The black solid and dashed lines denote the pre-multiplied spectra from DNS of the downward flow and upward flow respectively; the lines represent 75 %, 50 % and 5 % of the maximum energy in the spectrum.

gravity, compared with figure 5(b). However, for upward flow, figure 7(b), the whole plot is shifted to the right compared with the downward flow. This indicates that the main effect of gravity at this frequency is to amplify the energy of long structures for the upward flow and reduce it for the downward flow.

The combined effect of gravity and inertia is shown in the middle row of figure 7 for the same *St*, *Fr* and frequency settings. The energy gain ratio is very similar to the dusty gas model (top row), probably because of the very low *St*. This means that, at least for these parameter settings, the gravitational forces (rather than inertia) seem to dominate in determining the characteristics of the resolvent operator. As for figure 5, the corresponding pre-multiplied DNS spectra are superimposed on the resolvent gains. The overall trends of the spectra and gain plots are similar, with the downward flow being more energetic for smaller wavelengths, compared with the upward flow (compare dashed and solid contour lines). The location of the peak is fairly well reproduced, but it is somewhat more accurate for the downward flow. In figure 7(a–d) we have used $\alpha = 0$, $\beta = 1$, but the spectra do not change significantly if $\alpha = 1$. Marchioli *et al.* (2007) observed that, for low Stokes numbers ($St^+ = 1$), there is almost no difference between upward and downward flow

Mode type	k_z	λ_z^+	k_θ	λ_θ^+	c_w
Representative mode ($y_v^+ = 15$)	$\pi/2$	753.6	7	161.5	$\bar{u}_z(y_v^+ = 15)$
Representative mode ($y_v^+ = 30$)	$\pi/2$	753.6	7	161.5	$\bar{u}_z(y_v^+ = 30)$
Representative mode ($y_v^+ = 160$)	1	1310	1	1310	$\bar{u}_z(y_v^+ = 160)$
Locally clustered mode ($y_v^+ = 15$)	10π	37.7	10	113.1	$\bar{u}_z(y_v^+ = 15)$

Table 2. Wavenumber and wave speed combinations.

inside a channel unless one accounts for lift forces acting on the particles. However, they performed their numerical simulations for $Fr \approx \pm 14$ (defined using the bulk velocity and the channel half-height and computed using the data provided in the paper). In our case, for the larger value of $|Fr| = 4$, the effects of gravity are also negligible and there is almost no difference between upward and downward flow; this is shown in the mean and r.m.s. plots of figure 3.

In the last row of figure 7, panels (*e*) and (*f*), we plot the energy gain ratio of the simplified system, (5.32), for downward and upward flow, respectively. Now gravity affects the spectra because St/Fr_z appears in A_{c_5}. The trend is the same to the full resolvent operator, which indicates that the simplified system is capable of predicting qualitatively the effects of gravity on the particle behaviour.

6.2. *Mode shapes*

We now analyse the shapes of the response modes of the resolvent operator, (5.10), and explore the effect of *St* and Fr_z. Table 2 shows the wavelengths and wave speeds of the investigated modes. The first three rows refer to the 'representative modes', with wavenumber combinations close to the peak of the energy gain ratio. The wavenumbers are smaller for the third mode to account for the fact that the low-rank zone of the gain ratio also changes to lower wavenumbers at this wave speed. For a given wall normal distance *y*, the frequency ω is selected to satisfy $c_w = \bar{u}_z(y)$, thus enforcing *y* to be at the velocity critical layer i.e. $y = y_v$. The open circle in figure 5(*a*) denotes the location of the first representative mode examined, with $c_w = \bar{u}_z(y_v^+ = 15)$. The bottom row refers to a 'locally clustered' mode that has a relatively small wavelength; its location is marked by an asterisk in figure 5(*a*). Also, since $Fr_z = \pm 4$ has little effect on the statistics (refer to § 4) only $Fr_z = \pm 0.4$, as well as the no-gravity case $1/Fr_z = 0$, are considered. In the following, we plot $\sigma_1|\hat{\psi}_{1,c}(r; \boldsymbol{k})|$ to show the shape of the mode and the amplitude of the response.

The modes are shown in figure 8. The weights used are $\alpha = 0$, $\beta = 1$, but setting $\alpha = 1$ and $\beta = 0$ does not change the mode shapes significantly. For the no-gravity case (top row), the modes peak around the critical layer location as anticipated (there is a slight deviation for the third representative mode). Since $y_c = y_v$ for $1/Fr_z = 0$, the location of the peak is independent of St^+. The velocity modes (not shown) have a similar shape to the concentration modes; this has also been observed in other types of flow, such as boundary layers (Dawson *et al.* 2018; Dawson & McKeon 2020). The main effect of increasing the Stokes number is to (slightly) suppress the amplitude of the representative modes that have larger wavelengths, see panels (*a*), (*b*) and (*c*) and amplify the locally clustered modes, see panel (*d*).

On the other hand, gravity affects the modes significantly. For downward flows (middle row) $y_c < y_v$ (because y_c is determined from $c_w = \bar{u}_z(y_c) + St/Fr_z$ and $Fr_z > 0$) thus the
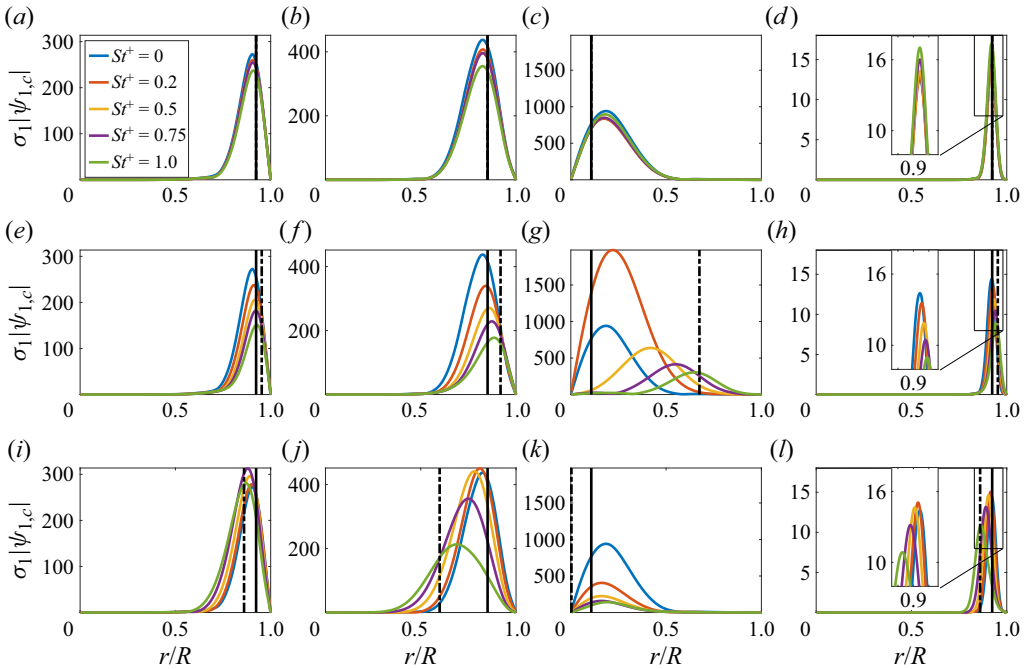
Figure 8. Response mode shapes for particle concentration fluctuations for no gravity in the top row (*a–d*), downward flow in the middle row (*e–h*) and upward flow in the bottom row (*i–l*). The first (*a,e,i*), second (*b,f,j*) and third columns (*c,g,k*) from left refer to representative modes with $c_w = \bar{u}_z(y_v^+ = 15)$, $c_w = \bar{u}_z(y_v^+ = 30)$, $c_w = \bar{u}_z(y_v^+ = 160)$, respectively. The right column (*d,h,l*) refers to the locally clustered mode. For more details, see table 2. To facilitate comparison, the scales of the vertical axes for the plots within each column are the same. The black vertical line indicates y_v (critical layer of the velocity field) and the dashed-dotted vertical line indicates y_c (critical layer of the concentration field) for $St^+ = 1$.

location of the concentration critical layer (denoted by a dashed vertical line) moves closer to the wall as St^+ increases. For small St^+ the modes peak close to $y_c \approx y_v$ (because St/Fr_i is small), but as St^+ increases, the difference $y_c - y_v$ grows and the modes peak closer to y_c. This trend can be seen in all panels in the middle row, but perhaps more clearly so in panel (*g*) where $y_v^+ (= 160)$ is furthest away from the wall. The clustered modes follow the same trend, but because the examined velocity critical layer $y_v^+ (= 15)$ is already close to the wall, the effect is not as dramatic. The amplitude of the representative modes is reduced close to the wall as St^+ increases; see panels (*e*) and (*f*). In panel (*g*), the modes peak further from the wall, the behaviour is more involved, but for high St^+ the amplitude is also reduced.

For upward flow (bottom row) $y_c > y_v$ (because $Fr_z < 0$) and the mode peaks move away from the wall as St^+ increases, following the shift of y_c; see panels (*i*) and (*j*). The trend is similar for the locally clustered mode; see (*l*). For the representative mode with $y_v^+ = 160$, panel (*k*), the velocity critical layer is already far from the wall, and the equation $c_w = \bar{u}_z(y_c) + St/Fr_z$ does not have a solution. Therefore, the effect of the upward gravity is to move the peak away from the wall, thereby increasing the mode amplitude in this region compared with the downward and no-gravity flow.

This plot also reveals that gravity amplifies the effect of inertia. This can be seen by observing the peak values across columns. For example, in the no-gravity case, the amplitude variation for the different St^+ is small (for all modes considered), while it is
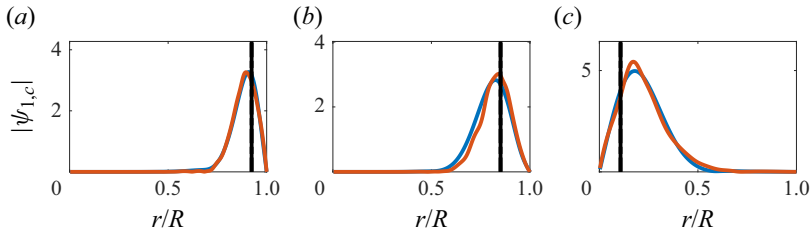
Figure 9. Response mode shapes for particle concentration fluctuations using the concentration profile from the present DNS (blue) and the profile from Sardina *et al.* (2011) (red) for $St^+ = 1$ and no gravity. The left (*a*), middle (*b*) and right (*c*) plot refer to representative modes with $c_w = \bar{u}_z(y_v^+ = 15)$, $c_w = \bar{u}_z(y_v^+ = 30)$, $c_w = \bar{u}_z(y_v^+ = 160)$, respectively, see table 2. The black vertical line indicates the location y_v of the critical layer of the velocity field.

much larger for the upward and downward flow cases. This observation on the interaction between gravity and inertia is consistent with the r.m.s. particle concentration shown in the right column of figure 3. When gravity is weak, panel (*b*), the effect of inertia is small, but when gravity is stronger, panel (*d*), the effect of inertia is significantly amplified.

In order to test the robustness of the obtained results, we have repeated the calculations using the concentration profile $\bar{c}_h(r)$ from figure 3 of Sardina *et al.* (2011). The profile was obtained from a Lagrangian simulation of $St^+ = 1$ particles using reflecting (bouncing) walls and without the effect of gravity. Comparison of the amplitudes of the first response modes for the three y_v^+ locations of table 2 are shown in figure 9. There are small differences between the modes using the different mean concentration profiles. Note that $\bar{c}_h(r)$ and its derivative $\partial \bar{c}_h(r)/\partial r$ appear only in the off-diagonal block A_{c_2} of the particle concentration equation, see (5.14). The frequency ω was selected so that $c_w = \bar{u}_z(y_v)$, which minimises the diagonal block A_{c_5}. The response is therefore mainly determined by this diagonal block and, as expected, it peaks at $y = y_v$ (recall that $y_c = y_v$, as gravity is absent). However, this block is independent of the profile $\bar{c}_h(r)$ and this explains the small difference in the responses shown in figure 9.

All the above results were obtained by tuning the frequency ω to satisfy $c_w = \bar{u}_z(y_v)$ for a given y_v. This was done in order to compare the different modes for the three gravity cases. Strictly speaking, however, in order to find the maximum response, ω should have been tuned separately for each gravity case to satisfy $c_w = \bar{u}_z(y_c) + St/Fr_z$ for a given y_c. In order to get a more complete picture, we focus on the first representative mode of table 2, with fixed $k_z = \pi/2$, $k_\theta = 7$ and $St^+ = 1$, and we vary ω such that the wave speed normalised with the centreline velocity is in the region $c_w/\bar{u}_{z,r=0} = 0 - 1.2$. Contour plots of $|\sigma_1 \hat{\psi}_{1,c}|$ are plotted in figure 10 for no gravity (left column), downward (middle column) and upward flow (right column) for the simplified resolvent operator (top row), and the full resolvent operator with $\alpha = 0$ and $\beta = 1$ (bottom row). For the simplified resolvent operator, the areas of highest amplitude closely follow the pipe's velocity profile, $\bar{u}_z(r)$, when gravity is omitted. For the downward and upward flows, the high values are concentrated around $\bar{u}_z(r) + St/Fr_z$, which can be larger or smaller than $\bar{u}_z(r)$, depending on the flow direction with respect to gravity. The results shown on the bottom row (from the full resolvent operator) are more nuanced. For the no-gravity case, the differences are small, but when gravity is taken into account, the areas of large activity are located between $\bar{u}_z(r)$ and $\bar{u}_z(r) + St/Fr_z$ (solid and dashed/dashed-dotted lines, respectively). It is very interesting to note that, for upward flow, the peak is sharper and moves closer to the wall in comparison with the no-gravity case, compare panels (*d*) and (*f*).
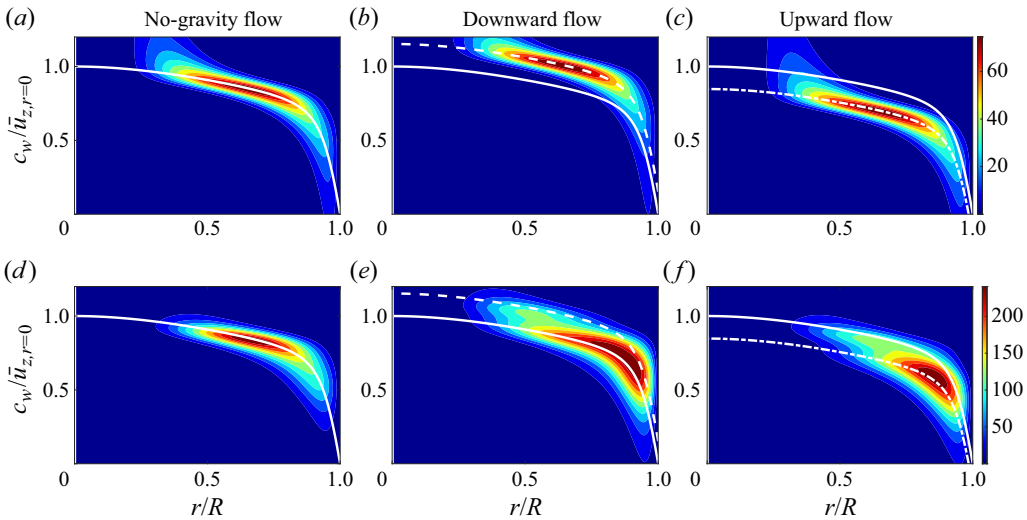
985 A27-22

Figure 10. Contour plots of $|\sigma_1 \hat{\psi}_{1,c}|$ in the (r, c_w) plane for $k_z = \pi/2$, $k_\theta = 7$, for (left column, *a,d*) no gravity, (middle column, *b,e*) downward flow, (right column, *c,f*), upward flow using the simplified operator (5.32) (top row, *a–c*) and the full resolvent operator with weights $\alpha = 1$, $\beta = 0$, (bottom row, *d–f*). The solid white line denotes $\bar{u}_z(r)$, while the dashed line denotes $\bar{u}_z(r) + St/Fr_z$ for the downward flow ($Fr_z > 0$), and the dashed-dotted line $\bar{u}_z(r) + St/Fr_z$ for the upward flow ($Fr_z < 0$).

Note also that the simplified resolvent operator, panel (*c*), cannot capture this shift towards the wall. For the downward flow, panel (*e*), the active areas are broader covering a larger region that, most importantly, penetrates to the core of the flow, closer to the centreline, compare with panel (*d*).

An increase in particle concentration fluctuation in the bulk region for downward flows and near the wall for an upward flow was also found in the Lagrangian simulations by Nilsen *et al.* (2013); refer to figure 7 in this paper, where the normalised variance of the Voronoi areas is plotted against y^+. An explanation offered by the authors is that a particle falling in downward flow is more likely to be swept away by a vortex that is translating with a velocity closer to that of the particle. Because the particle is moving faster than the fluid, the faster moving vortices closer to the centre will have more time to sweep the particles than the slower ones closer to the wall. The resolvent analysis allows us to offer an alternative interpretation for the effect of gravity on local particle concentration fluctuations. As evidenced in figure 10, this effect can be explained by the shift of the peak of the most amplified mode of the resolvent operator. Recall that this shift was obtained with (the rather crude) uniform broadband forcing, and was extracted directly from the governing equations, an observation that may allow in the future the derivation of new scaling relations, as in single phase flows; see Moarref *et al.* (2013).

It is important to recall that figure 10 is obtained for a particular set of wavenumbers (that are, however, judiciously selected). We repeated the analysis for other wavenumber pairs and similar results were obtained (plots not included for brevity). Strictly speaking, to examine the effect of gravity the most amplified response should be integrated over all wavenumbers and frequencies. Nevertheless, simplified as it is, this plot can also explain the shape of the r.m.s. plot in figure 3(*d*). For downward flow, the r.m.s. of particle concentration is larger near the bulk when compared with the upward flow, and the upward flow has a peak slightly closer to the wall, consistent with figures 10(*e*) and 10(*f*).
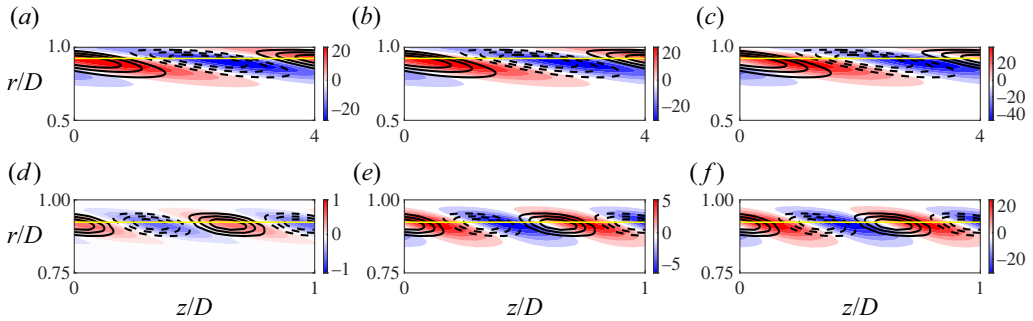
Figure 11. Contour plots of particle concentration response modes in the (r, z) plane for the no-gravity case with Neumann boundary conditions and $c_w = \bar{u}(y^+ = 15)$. The left column (a,d) is $St^+ = 0$, the middle column (b,e) is $St^+ = 0.2$ and the right column (c,f) is $St^+ = 1$. The top row panels $(a–c)$ refer to the representative mode, and the bottom row panels $(d–f)$ to the locally clustered mode, see table 2 for details. The horizontal yellow line indicates the critical layer y_v. Solid and dashed lines superimposed on the filled contours show positive and negative streamwise velocity fluctuations, respectively.

6.3. *Interaction of particle concentration with near-wall vortices*

In this section we focus on the effect of near-wall structures on the distribution of particle concentration. An observation often made in experiments and simulations with dilute particle-laden wall-bounded flows is that particles cluster near the wall, see Ninto & Garcia (1996), Fong *et al.* (2019), Marchioli & Soldati (2002) and Sardina *et al.* (2012), and preferentially accumulate in the low-speed near-wall streaks, where they are ejected away from the wall. We will analyse the mechanism responsible through the lens of the resolvent framework. For simplicity, we assume that gravity is absent, $1/Fr_i = 0$ and there is no wall deposition (hence, in the following, we use $\bar{c}$ and c', instead of $\bar{c}_h$ and c'_h). The latter assumption is implemented using a Neumann boundary condition for c' at the wall, i.e. $\partial c'/\partial r|_{r=1/2} = 0$. Also, in order to be as close as possible to conditions in the literature, we use again the mean concentration profile $\bar{c}(r)$ for $St^+ = 1$ of Sardina *et al.* (2011) that was obtained using Lagrangian simulations.

Contour plots of the particle concentration mode in the (z, r) and (x, y) planes are shown in figures 11 and 12, respectively. The top row refers to the first representative mode and the bottom row to the locally clustered modes, see table 2 for details. Lines, representing streamwise velocity fluctuations, are superimposed on the concentration plots. When the Stokes number increases (from the left to right column), the phase between the velocity and concentration fluctuations shifts, and negative streamwise velocity fluctuations start to overlap with the positive concentration fluctuations. This is more clearly observed for the smaller structures, see bottom row panels $(d–f)$ compared with the larger structures, top row panels $(a–c)$ and it is more noticeable in the (z, r) plane. The fact that it is more pronounced in the small scales is due to the pronounced presence of locally clustered modes with increasing Stokes number.

The theoretical explanation for this shift is due to the presence of one particular term in the particle concentration equation. Omitting the diffusion term, (2.7) can be written as

$$\frac{\partial c}{\partial t} + \boldsymbol{v} \cdot (\nabla c) + c(\nabla \cdot \boldsymbol{v}) = 0, \tag{6.1}$$
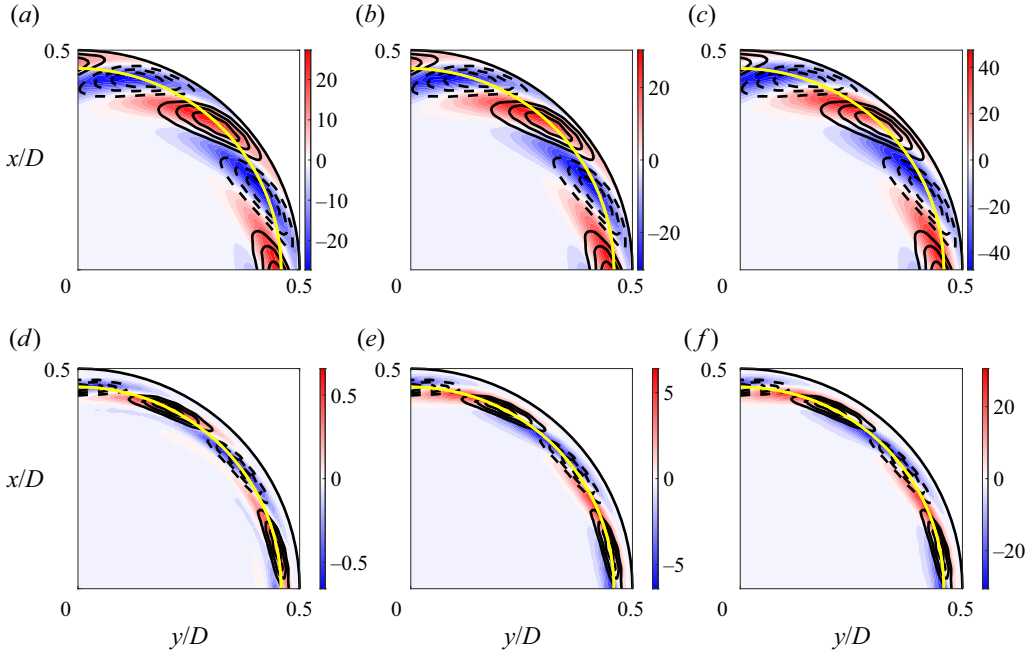
Figure 12. Contour plots of particle concentration response modes in the cross-stream (x, y) plane (only a quarter is shown) for the no-gravity case with Neumann boundary conditions and $c_w = \bar{u}(y^+ = 15)$. Left column (a,d) is $St^+ = 0$, middle column (b,e) is $St^+ = 0.2$ and right column (c,f) is $St^+ = 1$. The top row panels (a–c) refer to the representative mode and the bottom row (d–f) to the locally clustered mode, see table 2 for details. The solid yellow line marks the location of the critical layer y_v. Solid and dashed lines superimposed on the filled contours show positive and negative streamwise velocity fluctuations, respectively.

where $\boldsymbol{\nabla} \cdot \boldsymbol{v} \neq 0$. For $St = 0$, $\boldsymbol{v} = \boldsymbol{u}$ and the third term is 0 due to the incompressibility condition. However, for inertial particles we instead have

$$\boldsymbol{\nabla} \cdot \boldsymbol{v} = \frac{\partial}{\partial x_i}\left(u_i - St\frac{\mathrm{D}u_i}{\mathrm{D}t}\right) = -St\frac{\partial}{\partial x_i}\left(u_j\frac{\partial u_i}{\partial x_j}\right) = -St\frac{\partial u_j}{\partial x_i}\frac{\partial u_i}{\partial x_j}. \qquad (6.2)$$

We now, as usual, apply Reynolds decomposition in velocity and particle concentration fluctuations and substitute in (6.1) and (6.2). In polar coordinates, we can then write (see also 5.7)

$$\boldsymbol{v} \cdot (\boldsymbol{\nabla}c) = \bar{\boldsymbol{v}} \cdot (\boldsymbol{\nabla}\bar{c}) + \frac{\partial c'}{\partial z}\bar{u}_z + \frac{\partial \bar{c}}{\partial r}\left(u'_r - St\frac{\partial u'_r}{\partial t} - St\bar{u}_z\frac{\partial u'_r}{\partial z}\right) + \cdots, \qquad (6.3)$$

$$c(\boldsymbol{\nabla} \cdot \boldsymbol{v}) = \bar{c}(\boldsymbol{\nabla} \cdot \bar{\boldsymbol{v}}) - 2St\bar{c}\frac{\partial \bar{u}_z}{\partial r}\frac{\partial u'_r}{\partial z} + \cdots, \qquad (6.4)$$

where only the linear terms are explicitly shown. The only term that includes the effect of velocity shear on particle concentration appears in (6.4). This term arises from the linearisation of the divergence of the particle velocity field (6.2) and is the one responsible for the phase shift. The reason for this is that both $\bar{c}(r)$ and $\partial \bar{u}_z/\partial r$ are maximised in the viscous sublayer (see profile of $\bar{c}(r)$ in Sardina *et al.* 2011). Also the presence of $\partial u'_r/\partial z$ explains why the shift is strongest for larger wavenumbers (small structures). On the other hand, the factors $(\partial \bar{c}/\partial r)(r)$ and $\bar{u}_z(r)$ that appear in (6.3) tend to cancel each other because they peak at different regions (the former peaks at the wall, the latter at the centreline).

985 A27-25

7. Conclusions

We investigate particle transport and deposition in a turbulent pipe flow at $Re = 5300$ (based on bulk velocity) using the equilibrium Eulerian model and the resolvent framework. The resolvent operator, derived and applied for the first time in particle-laden flows, allows for the analysis of the effect of Stokes and Froude numbers on preferential particle concentration directly from the governing equations. Even with the simplest type of forcing (unit broadband forcing), the predicted spectra of the concentration fluctuations match well with the DNS spectra. The effect of Stokes number is to shift the spectra to smaller wavelengths, indicative of particle clustering. The effect of gravity was also explored. Gravity causes the critical layers for velocity and particle concentration to be at different locations. Inspection of the results shows that larger concentration fluctuations shift closer to the wall in upward flow; this is consistent with Voronoi analysis of particle locations reported in the literature.

Reflective (Neumann) boundary conditions and a mean concentration profile from the literature were also used to evaluate the ability of the developed framework to capture the effect of near-wall structures on preferential particle concentration. As St grows, regions with high particle concentration tend to overlap with negative velocity fluctuations. This is consistent with the correlation between low-speed streaks and long particle clusters that has been identified using Lagrangian simulations and reported multiple times in the literature. This phase shift was explained by inspection of the terms appearing in the resolvent operator. Indeed, the term responsible is due to the non-divergence of the particle velocity field. The explicit expression of this term links the mean concentration and shear stress profiles that are maximised in the same near-wall region.

We showed that the resolvent operator can provide useful insights that are consistent with Lagrangian simulations even using a model of limited range of validity for the velocity of the particle phase (Eulerian equilibrium model) and a simplified form of forcing. Most importantly, construction of the operator and evaluation of its singular values are computationally inexpensive operations. The fact that the maximum amplification is around the critical layer of particle concentration can potentially lead to new scaling laws, as in single-phase flows.

Future work can focus on applying the framework to Eulerian dispersion models that are valid for higher St^+. Comparisons with spectra and PDFs from Voronoi analysis of Lagrangian simulations would be very interesting. Are the statistics of particle clusters and voids the same? What is the effect of forcing? Is accurate forcing needed? It would be revealing also to apply to flows with large mass fraction of the particulate phase and explore the effect on the carrier phase; the Eulerian equations for two-way coupling can be found in Shotorban & Balachandar (2009). Furthermore, the resolvent framework makes it easy to analyse the effect of very high Sc. One can use a mean concentration profile from Lagrangian simulations and explore the effect of Sc on the rank of the operator, most amplified modes, spectra etc.

Further insight can be obtained by probing the resolvent operator through input–output analysis. This would allow the exploration of the linear amplification mechanisms from the forcing of one field to the response of another; see for instance Jovanović & Bamieh (2005), Jeun, Nichols & Jovanović (2016) and Jovanović (2021). This approach can lead to physics-based optimisation, an example for heat transfer enhancement can be found in Herrmann-Priesnitz et al. (2018), and it can also be applied directly to particulate flows.

There is another important research direction well worth exploring. Is it possible to extract the resolvent operator directly from Lagrangian simulations? That would make this approach applicable to much larger St that cannot be reached with Eulerian models. We

believe that the answer is yes. One can apply recently developed data-driven methods, such as the one proposed in Herrmann *et al.* (2021), directly to snapshots of the Voronoi concentration fields (Eulerian fields that can be obtained from the Lagrangian particle positions at every time step). It is hoped that this approach will provide a fresh, and hopefully useful, perspective to analyse a wide range of particle-laden two-phase flows, with far reaching implications for their reduced-order modelling, control etc. We acknowledge, however, that the application of such methods is challenging and still an open, active research topic even for single-phase flows, but any development can be directly transferred to multiphase flows.

Author ORCIDs.
Stelios Rigopoulos https://orcid.org/0000-0002-0311-2070;
George Papadakis https://orcid.org/0000-0003-0594-3107.

Appendix A. Derivation of the Fourier-transformed equation for the particle concentration fluctuations

Substituting in (5.2) expression (2.5) for the particle velocities of the equilibrium Eulerian model we get

$$
\begin{aligned}
\frac{\partial c_h}{\partial t} &+ \frac{1}{r}\frac{\partial}{\partial r}\left\{ r\left[u_r - St\left(\frac{\partial u_r}{\partial t} + u_r\frac{\partial u_r}{\partial r} + \frac{u_\theta}{r}\frac{\partial u_r}{\partial \theta} - \frac{u_\theta^2}{r} + u_z\frac{\partial u_r}{\partial z} \right) \right] c_h \right\} \\
&+ \frac{1}{r}\frac{\partial}{\partial \theta}\left\{ \left[u_\theta - St\left(\frac{\partial u_\theta}{\partial t} + u_r\frac{\partial u_\theta}{\partial r} + \frac{u_\theta}{r}\frac{\partial u_\theta}{\partial \theta} + \frac{u_\theta u_r}{r} + u_z\frac{\partial u_\theta}{\partial z} \right) \right] c_h \right\} \\
&+ \frac{\partial}{\partial z}\left\{ \left[u_z + \frac{St}{Fr_z} - St\left(\frac{\partial u_z}{\partial t} + u_r\frac{\partial u_z}{\partial r} + \frac{u_\theta}{r}\frac{\partial u_z}{\partial \theta} + u_z\frac{\partial u_z}{\partial z} \right) \right] c_h \right\} \\
&= \frac{1}{ReSc}\left[\frac{1}{r}\frac{\partial}{\partial r}\left(r\frac{\partial c_h}{\partial r} \right) + \frac{1}{r^2}\frac{\partial^2 c_h}{\partial \theta^2} + \frac{\partial^2 c_h}{\partial z^2} \right] + S_{c_h},
\end{aligned}
\tag{A1}
$$

where it is assumed that the gravity vector in the streamwise direction. Using Reynolds decomposition $q = \bar{q} + q'$ and applying $\bar{u}_\theta = \bar{u}_r = \partial\bar{u}_z/\partial t = \partial\bar{u}_z/\partial\theta = \partial\bar{u}_z/\partial z = 0$ we get

$$
\frac{\partial(\bar{c}_h + c_h')}{\partial t}
$$

$$
+ \frac{1}{r}\frac{\partial}{\partial r}\left\{ r\left[u_r' - St\left(\frac{\partial u_r'}{\partial t} + u_r'\frac{\partial u_r'}{\partial r} + \frac{u_\theta'}{r}\frac{\partial u_r'}{\partial \theta} - \frac{u_\theta^{2'}}{r} + (\bar{u}_z + u_z')\frac{\partial u_r'}{\partial z} \right) \right] (\bar{c}_h + c_h') \right\}
$$

$$
+ \frac{1}{r}\frac{\partial}{\partial\theta}\left\{\left[u'_\theta - St\left(\frac{\partial u'_\theta}{\partial t} + u'_r\frac{\partial u'_\theta}{\partial r} + \frac{u'_\theta}{r}\frac{\partial u'_\theta}{\partial\theta} + \frac{u'_\theta u'_r}{r} + (\bar{u}_z + u'_z)\frac{\partial u'_\theta}{\partial z}\right)\right](\bar{c}_h + c'_h)\right\}
$$

$$
+ \frac{\partial}{\partial z}\left\{\left[(\bar{u}_z + u'_z) + \frac{St}{Fr_z} - St\left(\frac{\partial u'_z}{\partial t} + u'_r\frac{\partial(\bar{u}_z + u'_z)}{\partial r} + \frac{u'_\theta}{r}\frac{\partial u'_z}{\partial\theta}\right.\right.\right.
$$

$$
\left.\left.\left.+ (\bar{u}_z + u'_z)\frac{\partial u'_z}{\partial z}\right)\right](\bar{c}_h + c'_h)\right\}
$$

$$
= \frac{1}{ReSc}\left[\frac{1}{r}\frac{\partial}{\partial r}\left(r\frac{\partial(\bar{c}_h + c'_h)}{\partial r}\right) + \frac{1}{r^2}\frac{\partial^2(\bar{c}_h + c'_h)}{\partial\theta^2} + \frac{\partial^2(\bar{c}_h + c'_h)}{\partial z^2}\right] + S_{c_h}. \tag{A2}
$$

Subtracting the time average of the above equation and keeping the terms that are linear with respect to the velocity and concentration fluctuations on the left-hand side we obtain

$$
\frac{\partial c'_h}{\partial t} + \frac{1}{r}\frac{\partial}{\partial r}\left\{r\left[u'_r\bar{c}_h + St\left(-\frac{\partial u'_r}{\partial t}\bar{c}_h - \bar{u}_z\frac{\partial u'_r}{\partial z}\bar{c}_h\right)\right]\right\}
$$

$$
+ \frac{1}{r}\frac{\partial}{\partial\theta}\left[u'_\theta\bar{c}_h + St\left(-\frac{\partial u'_\theta}{\partial t}\bar{c}_h - \bar{u}_z\frac{\partial u'_\theta}{\partial z}\bar{c}_h\right)\right]
$$

$$
+ \frac{\partial}{\partial z}\left[u'_z\bar{c}_h + \bar{u}_z c'_h + St\left(\frac{1}{Fr_z}c'_h - \frac{\partial u'_z}{\partial t}\bar{c}_h - u'_r\frac{\partial\bar{u}_z}{\partial r}\bar{c}_h - \bar{u}_z\frac{\partial u'_z}{\partial z}\bar{c}_h\right)\right]
$$

$$
- \frac{1}{ReSc}\left[\frac{1}{r}\frac{\partial}{\partial r}\left(r\frac{\partial c'_h}{\partial r}\right) + \frac{1}{r^2}\frac{\partial^2 c'_h}{\partial\theta^2} + \frac{\partial^2 c'_h}{\partial z^2}\right] - S'_{c_h} = f_c, \tag{A3}
$$

where

$$
S'_{c_h} = a\left[\bar{u}_z c'_h + u'_z\bar{c}_h + \frac{St}{Fr_z}c'_h - St\left(u'_r\frac{\partial\bar{u}_z}{\partial r}\bar{c}_h + \bar{u}_z\frac{\partial u'_z}{\partial z}\bar{c}_h\right)\right] + \frac{1}{ReSc}\left[-2a\frac{\partial c'_h}{\partial z} + a^2 c'_h\right], \tag{A4}
$$

is the fluctuating source term S'_{c_h} and all the nonlinear terms are included in f_c. The term S'_{c_h} can be written in more compact form as

$$
S'_{c_h} = \Theta_{s,z}(u'_z) + \Theta_{s,r}(u'_r) + \Theta_{s,c}(c'_h), \tag{A5}
$$

where $\Theta_{s,z}$, $\Theta_{s,r}$ and $\Theta_{s,c}$ are operators acting on u'_z, u'_r and c'_h respectively, i.e.

$$
\Theta_{s,z}(u'_z) = a\left(u'_z\bar{c}_h - St\bar{u}_z\bar{c}_h\frac{\partial u'_z}{\partial z}\right), \tag{A6}
$$

$$
\Theta_{s,r}(u'_r) = -aSt u'_r\frac{\partial\bar{u}_z}{\partial r}\bar{c}_h, \tag{A7}
$$

$$
\Theta_{s,c}(c'_h) = a\left[\bar{u}_z c'_h + \frac{St}{Fr_z}c'_h + \frac{1}{ReSc}\left(-2\frac{\partial c'_h}{\partial z} + ac'_h\right)\right]. \tag{A8}
$$

Expanding (A3), where we once again assume that the flow is homogeneous in the azimuthal and streamwise directions, thus removing any term containing $\partial\bar{u}_z/\partial\theta$, $\partial\bar{u}_z/\partial z$,

985 A27-28

$\partial \bar{c}_h/\partial\theta$ or $\partial \bar{c}_h/\partial z$, we obtain

$$
\frac{\partial c_h'}{\partial t} + u_r'\frac{\partial \bar{c}_h}{\partial r} + \bar{c}_h\frac{\partial u_r'}{\partial r}
$$

$$
+ St\left(-\frac{\partial^2 u_r'}{\partial t\partial r}\bar{c}_h - \frac{\partial \bar{c}_h}{\partial r}\frac{\partial u_r'}{\partial t} - \frac{\partial \bar{u}_z}{\partial r}\frac{\partial u_r'}{\partial z}\bar{c}_h - \bar{u}_z\frac{\partial^2 u_r'}{\partial z\partial r}\bar{c}_h - \bar{u}_z\frac{\partial u_r'}{\partial z}\frac{\partial \bar{c}_h}{\partial r}\right)
$$

$$
+ \frac{1}{r}\left[u_r'\bar{c}_h + St\left(-\frac{\partial u_r'}{\partial t} - \bar{u}_z\frac{\partial u_r'}{\partial z}\right)\bar{c}_h\right] + \frac{1}{r}\left[\bar{c}_h\frac{\partial u_\theta'}{\partial\theta} + St\left(-\frac{\partial^2 u_\theta'}{\partial t\partial\theta}\bar{c}_h - \bar{u}_z\frac{\partial^2 u_\theta'}{\partial z\partial\theta}\bar{c}_h\right)\right]
$$

$$
+ \bar{c}_h\frac{\partial u_z'}{\partial z} + \bar{u}_z\frac{\partial c_h'}{\partial z} + St\left(\frac{1}{Fr_z}\frac{\partial c_h'}{\partial z} - \frac{\partial^2 u_z'}{\partial t\partial z}\bar{c}_h - \frac{\partial u_r'}{\partial z}\frac{\partial \bar{u}_z}{\partial r}\bar{c}_h - \bar{u}_z\frac{\partial^2 u_z'}{\partial z\partial z}\bar{c}_h\right)
$$

$$
- \frac{1}{ReSc}\left[\frac{1}{r}\frac{\partial}{\partial r}\left(r\frac{\partial c_h'}{\partial r}\right) + \frac{1}{r^2}\frac{\partial^2 c_h'}{\partial\theta^2} + \frac{\partial^2 c_h'}{\partial z^2}\right] - S_{c_h}' = f_c. \tag{A9}
$$

The continuity equation in polar coordinates is $CE = \partial u_r'/\partial r + u_r'/r + (1/r)(\partial u_\theta'/\partial\theta) + \partial u_z'/\partial z = 0$, thus $\bar{c}_h \cdot (CE) = 0$, $\bar{c}_h \cdot (\partial(CE)/\partial t) = 0$ and $\bar{c}_h\,\bar{u}_z(\partial(CE)/\partial z) = 0$.

Applying Fourier transform to (A9) we obtain

$$
-\omega\mathrm{i}\hat{c}_h + \hat{u}_r\frac{\partial \bar{c}_h}{\partial r} + St\left(\mathrm{i}\omega\hat{u}_r\frac{\partial \bar{c}_h}{\partial r} - \mathrm{i}k_z\hat{u}_r\frac{\partial \bar{u}_z}{\partial r}\bar{c}_h - \mathrm{i}k_z\hat{u}_r\bar{u}_z\frac{\partial \bar{c}_h}{\partial r}\right)
$$

$$
+ \mathrm{i}k_z\hat{c}_h\bar{u}_z + St\left(\mathrm{i}k_z\hat{c}_h\frac{1}{Fr_z} - \mathrm{i}k_z\hat{u}_r\frac{\partial \bar{u}_z}{\partial r}\bar{c}_h\right) - \frac{1}{ReSc}\left[\frac{1}{r}\frac{\partial}{\partial r}\left(r\frac{\partial \hat{c}_h}{\partial r}\right) - \frac{1}{r^2}k_\theta^2\hat{c}_h - k_z^2\hat{c}_h\right]
$$

$$
- [\Theta_{s,z}(\hat{u}_z) + \Theta_{s,r}(\hat{u}_r) + \Theta_{s,c}(\hat{c}_h)] = \hat{f}_c, \tag{A10}
$$

where the caret $\hat{}$ denotes a Fourier-transformed variable. This can be written in a more compact form as

$$
A_{c_1}\hat{u}_z + A_{c_2}\hat{u}_r + (-\mathrm{i}\omega + A_{c_5})\hat{c}_h = \hat{f}_c, \tag{A11}
$$

where

$$
A_{c_1} = -\Theta_{s,z}, \tag{A12}
$$

$$
A_{c_2} = \frac{\partial \bar{c}_h}{\partial r} + St\left(\mathrm{i}\omega\frac{\partial \bar{c}_h}{\partial r} - 2\mathrm{i}k_z\frac{\partial \bar{u}_z}{\partial r}\bar{c}_h - \mathrm{i}k_z\bar{u}_z\frac{\partial \bar{c}_h}{\partial r}\right) - \Theta_{s,r}, \tag{A13}
$$

$$
A_{c_5} = \mathrm{i}k_z\bar{u}_z - \frac{1}{ReSc}\left(\frac{1}{r}\frac{\partial}{\partial r} + \frac{\partial^2}{\partial r^2} - \frac{1}{r^2}k_\theta^2 - k_z^2\right) + \frac{St}{Fr_z}\mathrm{i}k_z - \Theta_{s,c}. \tag{A14}
$$

The operators A_{c_1}, A_{c_2} and A_{c_5} are inserted into matrix L of (5.11).

REFERENCES

AHMED, M.A., BAE, H.J., THOMPSON, A.F. & MCKEON, B.J. 2021 Resolvent analysis of stratification effects on wall-bounded shear flows. *Phys. Rev. Fluids* **6** (8), 1–25.

AIYER, A.K., YANG, D., CHAMECKI, M. & MENEVEAU, C. 2019 A population balance model for large eddy simulation of polydisperse droplet evolution. *J. Fluid Mech.* **878**, 700–739.

BALACHANDAR, S. & EATON, J.K. 2010 Turbulent dispersed multiphase flow. *Annu. Rev. Fluid Mech.* **42**, 111–133.

BALACHANDAR, S., ZALESKI, S., SOLDATI, A., AHMADI, G. & BOUROUIBA, L. 2020 Host-to-host airborne transmission as a multiphase flow problem for science-based social distance guidelines. *Intl J. Multiphase Flow* **132**, 103439.

BALAY, S., *et al.* 2022 PETSc/TAO users manual. *Tech. Rep.* ANL-21/39 - Revision 3.18. Argonne National Laboratory.

BRANDT, L. & COLETTI, F. 2022 Particle-laden turbulence: progress and perspectives. *Annu. Rev. Fluid Mech.* **54** (1), 159–189.

BROOKE, J.W., HANRATTY, T.J. & MCLAUGHLIN, J.B. 1994 Free-flight mixing and deposition of aerosols. *Phys. Fluids* **6** (10), 3404–3415.

CAPORALONI, M., TAMPIERI, F., TROMBETTI, F. & VITTORI, O. 1975 Transfer of particles in nonisotropic air turbulence. *J. Atmos. Sci.* **32**, 565–568.

CARRIER, G.F. 1958 Shock waves in a dusty gas. *J. Fluid Mech.* **4** (4), 376–382.

CERMINARA, M., ESPOSTI ONGARO, T. & BERSELLI, L.C. 2016 ASHEE-1.0: a compressible, equilibrium-Eulerian model for volcanic ash plumes. *Geosci. Model Develop.* **9** (2), 697–730.

DAWSON, S.T.M. & MCKEON, B.J. 2020 Prediction of resolvent mode shapes in supersonic turbulent boundary layers. *Intl J. Heat Fluid Flow* **85**, 108677.

DAWSON, S.T.M., SAXTON-FOX, T. & MCKEON, B.J. 2018 Modeling passive scalar dynamics in wall-bounded turbulence using resolvent analysis. In *2018 AIAA Fluid Dynamics Conference*, p. 4042. AIAA.

DRUZHININ, O.A. 1994 Concentration waves and flow modification in a particle-laden circular vortex. *Phys. Fluids* **6** (10), 3276–3284.

FALGOUT, R.D. & YANG, U.M. 2002 Hypre: a library of high performance preconditioners. In *Computational Science — ICCS 2002* (ed. P.M.A. Sloot, A.G. Hoekstra, C.J.K. Tan & J.J. Dongarra), pp. 632–641. Springer.

FERRY, J. & BALACHANDAR, S. 2001 A fast Eulerian method for disperse two-phase flow. *Intl J. Multiphase Flow* **27** (7), 1199–1226.

FERRY, J. & BALACHANDAR, S. 2002 Equilibrium expansion for the Eulerian velocity of small particles. *Powder Technol.* **125** (2), 131–139.

FERRY, J., RANI, S.L. & BALACHANDAR, S. 2003 A locally implicit improvement of the equilibrium Eulerian method. *Intl J. Multiphase Flow* **29** (6), 869–891.

FONG, K.O., AMILI, O. & COLETTI, F. 2019 Velocity and spatial distribution of inertial particles in a turbulent channel flow. *J. Fluid Mech.* **872**, 367–406.

FOX, R.O., LAURENT, F. & MASSOT, M. 2008 Numerical simulation of spray coalescence in an eulerian framework: direct quadrature method of moments and multi-fluid method. *J. Comput. Phys.* **227** (6), 3058–3088.

GUHA, A. 1997 A unified eulerian theory of turbulent deposition to smooth and rough surfaces. *J. Aerosol. Sci.* **28** (8), 1517–1537.

GUHA, A. 2008 Transport and deposition of particles in turbulent and laminar flow. *Annu. Rev. Fluid Mech.* **40** (1), 311–341.

HERRMANN, B., BADDOO, P.J., SEMAAN, R., BRUNTON, S.L. & MCKEON, B.J. 2021 Data-driven resolvent analysis. *J. Fluid Mech.* **918**, A10.

HERRMANN-PRIESNITZ, B., CALDERÓN-MUÑOZ, W.R., DIAZ, G. & SOTO, R. 2018 Heat transfer enhancement strategies in a swirl flow minichannel heat sink based on hydrodynamic receptivity. *Intl J. Heat Mass Transfer* **127**, 245–256.

ICARDI, M., MARCHISIO, D.L., CHIDAMBARAM, N. & FOX, R.O. 2013 Equilibrium-Eulerian les model for turbulent poly-dispersed particle-laden flow. *Intl J. Nonlinear Sci. Numer. Simul.* **14** (2), 139–158.

INCROPERA, F.P., DEWITT, D.P., BERGMAN, T.L. & LAVINE, A.S. 2007 *Fundamentals of Heat and Mass Transfer*, 6th edn. John Wiley & Sons.

JANE BAE, H., DAWSON, S.T.M. & MCKEON, B.J. 2019 Resolvent-based study of compressibility effects on supersonic turbulent boundary layers. *J. Fluid Mech.* **883**, 1–32.

JEUN, J., NICHOLS, J.W. & JOVANOVIĆ, M.R. 2016 Input-output analysis of high-speed axisymmetric isothermal jet noise. *Phys. Fluids* **28** (4), 047101.

JOVANOVIĆ, M.R. 2021 From bypass transition to flow control and data-driven turbulence modeling: an input–output viewpoint. *Annu. Rev. Fluid Mech.* **53** (1), 311–345.

JOVANOVIĆ, M.R. & BAMIEH, B. 2005 Componentwise energy amplification in channel flows. *J. Fluid Mech.* **534**, 145–183.

LEE, M.M., HANRATTY, T.J. & ADRIAN, R.J. 1989 The interpretation of droplet deposition measurements with a diffusion model. *Intl J. Multiphase Flow* **15** (3), 459–469.

LUHAR, M., SHARMA, A.S. & MCKEON, B.J. 2014 Opposition control within the resolvent analysis framework. *J. Fluid Mech.* **749**, 597–626.

MARBLE, F.E. 1970 Dynamics of dusty gases. *Annu. Rev. Fluid Mech.* **2**, 397–446.

MARCHIOLI, C., PICCIOTTO, M. & SOLDATI, A. 2007 Influence of gravity and lift on particle velocity statistics and transfer rates in turbulent vertical channel flow. *Intl J. Multiphase Flow* **33** (3), 227–251.

MARCHIOLI, C. & SOLDATI, A. 2002 Mechanisms for particle transfer and segregation in a turbulent boundary layer. *J. Fluid Mech.* **468**, 283–315.

MARTINI, E., CAVALIERI, A.V.G., JORDAN, P., TOWNE, A. & LESSHAFFT, L. 2020 Resolvent-based optimal estimation of transitional and turbulent flows. *J. Fluid Mech.* **900**, A2.

MAXEY, M.R. 1987 The gravitational settling of aerosol particles in homogeneous turbulence and random flow fields. *J. Fluid Mech.* **174**, 441–465.

MAXEY, M.R. & RILEY, J.J. 1983 Equation of motion for a small rigid sphere in a nonuniform flow. *Phys. Fluids* **26** (4), 883–889.

MCKEON, B.J. 2017 The engine behind (wall) turbulence: perspectives on scale interactions. *J. Fluid Mech.* **817**, 1–86.

MCKEON, B.J. & SHARMA, A.S. 2010 A critical-layer framework for turbulent pipe flow. *J. Fluid Mech.* **658**, 336–382.

MIKHAYLOV, K., RIGOPOULOS, S. & PAPADAKIS, G. 2021 Reconstruction of large-scale flow structures in a stirred tank from limited sensor data. *AIChE J.* **67**, e17348.

MOARREF, R., SHARMA, A.S., TROPP, J.A. & MCKEON, B.J. 2013 Model-based scaling of the streamwise energy density in high-Reynolds-number turbulent channels. *J. Fluid Mech.* **734**, 275–316.

MONCHAUX, R., BOURGOIN, M. & CARTELLIER, A. 2010 Preferential concentration of heavy particles: a Voronoï analysis. *Phys. Fluids* **22** (10), 103304.

MORRA, P., NOGUEIRA, P.A.S., CAVALIERI, A.V.G. & HENNINGSON, D.S. 2021 The colour of forcing statistics in resolvent analyses of turbulent channel flows. *J. Fluid Mech.* **907**, A24.

MORRA, P., SEMERARO, O., HENNINGSON, D.S. & COSSU, C. 2019 On the relevance of reynolds stresses in resolvent analyses of turbulent wall-bounded flows. *J. Fluid Mech.* **867**, 969–984.

NILSEN, C., ANDERSSON, H.I. & ZHAO, L. 2013 A Voronoï analysis of preferential concentration in a vertical channel flow. *Phys. Fluids* **25** (11), 115108.

NINTO, Y. & GARCIA, M.H. 1996 Experiments on particle–turbulence interactions in the near–wall region of an open channel flow: implications for sediment transport. *J. Fluid Mech.* **326**, 285–319.

OLIVEIRA, J.L.G., VAN DER GELD, C.W.M. & KUERTEN, J.G.M. 2013 Lagrangian and Eulerian statistics of pipe flows measured with 3D-ptv at moderate and high Reynolds numbers. *Flow Turbul. Combust.* **91** (1), 105–137.

OLIVEIRA, J.L.G., VAN DER GELD, C.W.M. & KUERTEN, J.G.M. 2017 Concentration and velocity statistics of inertial particles in upward and downward pipe flow. *J. Fluid Mech.* **822**, 640–663.

PICANO, F., SARDINA, G. & CASCIOLA, C.M. 2009 Spatial development of particle-laden turbulent pipe flow. *Phys. Fluids* **21** (9), 093305.

PILOU, M., TSANGARIS, S., NEOFYTOU, P., HOUSIADAS, C. & DROSSINOS, Y. 2011 Inertial particle deposition in a 90 laminar flow bend: an Eulerian fluid particle approach. *Aerosol. Sci. Technol.* **45** (11), 1376–1387.

POPE, S.B. 2000 *Turbulent Flows*, 1st edn. Cambridge University Press.

RANI, S.L. & BALACHANDAR, S. 2003 Evaluation of the equilibrium Eulerian approach for the evolution of particle concentration in isotropic turbulence. *Intl J. Multiphase Flow* **29** (12), 1793–1816.

REEKS, M.W. 1983 The transport of discrete particles in inhomogeneous turbulence. *J. Aerosol. Sci.* **14** (6), 729–739.

RICHTER, D. & CHAMECKI, M. 2018 Inertial effects on the vertical transport of suspended particles in a turbulent boundary layer. *Boundary-Layer Meteorol.* **167** (2), 235–256.

SARDINA, G., PICANO, F., SCHLATTER, P., BRANDT, L. & CASCIOLA, C.M. 2011 Large scale accumulation patterns of inertial particles in wall-bounded turbulent flow. *Flow Turbul. Combust.* **86** (3–4), 519–532.

SARDINA, G., SCHLATTER, P., BRANDT, L., PICANO, F. & CASCIOLA, C.M. 2012 Wall accumulation and spatial localization in particle-laden wall flows. *J. Fluid Mech.* **699** (2014), 50–78.

SCHLANDER, R.K., RIGOPOULOS, S. & PAPADAKIS, G. 2022 Analysis of wall mass transfer in turbulent pipe flow combining extended proper orthogonal decomposition and Fukugata-Iwamoto-Kasagi identity. *Phys. Rev. Fluids* **7**, 024603.

SCHLANDER, R.K., RIGOPOULOS, S. & PAPADAKIS, G. 2024 Role of flow structures on the deposition of low-inertia particles in turbulent pipe flow. *Phys. Rev. Fluids* **9**, 024303.

SHOTORBAN, B. & BALACHANDAR, S. 2009 Two-fluid approach for direct numerical simulation of particle-laden turbulent flows at small stokes numbers. *Phys. Rev.* E **79**, 056703.

SQUIRES, K.D. & EATON, J.K. 1991 Measurements of particle dispersion obtained from direct numerical simulations of isotropic turbulence. *J. Fluid Mech.* **226** (1961), 1–35.

STRAUB, S., FOROOGHI, P., MAROCCO, L., WETZEL, T., VINUESA, R., SCHLATTER, P. & FROHNAPFEL, B. 2019 The influence of thermal boundary conditions on turbulent forced convection pipe flow at two Prandtl numbers. *Intl J. Heat Mass Transfer* **144**, 118601.

TAGAWA, Y., MERCADO, J.M., PRAKASH, V.N., CALZAVARINI, E., SUN, C. & LOHSE, D. 2012 Three-dimensional Lagrangian Voronoï analysis for clustering of particles and bubbles in turbulence. *J. Fluid Mech.* **693**, 201–215.

THOMAREIS, N. & PAPADAKIS, G. 2018 Resolvent analysis of separated and attached flows around an airfoil at transitional Reynolds number. *Phys. Rev. Fluids* **3** (7), 073901.

TOWNE, A. & LOZANO-DURÁN, A. & YANG, X. 2020 Resolvent-based estimation of space-time flow statistics. *J. Fluid Mech.* **883**, A17SEP.

TREFETHEN, L.N. 2000 *Spectral Methods in MATLAB*. Society for Industrial and Applied Mathematics.

UIJTTEWAAL, W.S.J. & OLIEMANS, R.V.A. 1996 Particle dispersion and deposition in direct numerical and large eddy simulations of vertical pipe flows. *Phys. Fluids* **8** (10), 2590–2604.

VEENMAN, M.P.B. 2004 Statistical analysis of turbulent pipe flow: a numerical approach. PhD thesis, Eindhoven University of Technology.

WU, X. & MOIN, P. 2008 A direct numerical simulation study on the mean velocity characteristics in turbulent pipe flow. *J. Fluid Mech.* **608**, 81–112.

YANG, D., CHEN, B., SOCOLOFSKY, S.A., CHAMECKI, M. & MENEVEAU, C. 2016 Large-eddy simulation and parameterization of buoyant plume dynamics in stratified flow. *J. Fluid Mech.* **794**, 798–833.

YAO, H., MOLLICONE, J.-P. & PAPADAKIS, G. 2022 Analysis of interscale energy transfer in a boundary layer undergoing bypass transition. *J. Fluid Mech.* **941**, A14.

YAO, H. & PAPADAKIS, G. 2023 On the role of the laminar/turbulent interface in energy transfer between scales in bypass transition. *J. Fluid Mech.* **960**, A24.

YEH, C.-A. & TAIRA, K. 2019 Resolvent-analysis-based design of airfoil separation control. *J. Fluid Mech.* **867**, 572–610.

YOUNG, J. & LEEMING, A. 1997 A theory of particle deposition in turbulent pipe flow. *J. Fluid Mech.* **340**, 129–159.